



UNIVERSITAT_{DE}
BARCELONA

Spin crossover supramolecular coordination compounds: design, synthesis and properties

Mohanad D .Darawsheh

ADVERTIMENT. La consulta d'aquesta tesi queda condicionada a l'acceptació de les següents condicions d'ús: La difusió d'aquesta tesi per mitjà del servei TDX (www.tdx.cat) i a través del Dipòsit Digital de la UB (diposit.ub.edu) ha estat autoritzada pels titulars dels drets de propietat intel·lectual únicament per a usos privats emmarcats en activitats d'investigació i docència. No s'autoritza la seva reproducció amb finalitats de lucre ni la seva difusió i posada a disposició des d'un lloc aliè al servei TDX ni al Dipòsit Digital de la UB. No s'autoritza la presentació del seu contingut en una finestra o marc aliè a TDX o al Dipòsit Digital de la UB (framing). Aquesta reserva de drets afecta tant al resum de presentació de la tesi com als seus continguts. En la utilització o cita de parts de la tesi és obligat indicar el nom de la persona autora.

ADVERTENCIA. La consulta de esta tesis queda condicionada a la aceptación de las siguientes condiciones de uso: La difusión de esta tesis por medio del servicio TDR (www.tdx.cat) y a través del Repositorio Digital de la UB (diposit.ub.edu) ha sido autorizada por los titulares de los derechos de propiedad intelectual únicamente para usos privados enmarcados en actividades de investigación y docencia. No se autoriza su reproducción con finalidades de lucro ni su difusión y puesta a disposición desde un sitio ajeno al servicio TDR o al Repositorio Digital de la UB. No se autoriza la presentación de su contenido en una ventana o marco ajeno a TDR o al Repositorio Digital de la UB (framing). Esta reserva de derechos afecta tanto al resumen de presentación de la tesis como a sus contenidos. En la utilización o cita de partes de la tesis es obligado indicar el nombre de la persona autora.

WARNING. On having consulted this thesis you're accepting the following use conditions: Spreading this thesis by the TDX (www.tdx.cat) service and by the UB Digital Repository (diposit.ub.edu) has been authorized by the titular of the intellectual property rights only for private uses placed in investigation and teaching activities. Reproduction with lucrative aims is not authorized nor its spreading and availability from a site foreign to the TDX service or to the UB Digital Repository. Introducing its content in a window or frame foreign to the TDX service or to the UB Digital Repository is not authorized (framing). Those rights affect to the presentation summary of the thesis as well as to its contents. In the using or citation of parts of the thesis it's obliged to indicate the name of the author.

Contents

CHAPTER 4: Spin Crossover in Fe(II) Dimerized Mononuclear Triple-Stranded Helicates 135

4.1	Introduction	135
4.2	Synthesis and Crystal Structure of $\text{Cl} \subset [\text{Fe}(\text{H}_2\text{L4})_3]_2(\text{OH})(\text{PF}_6)_2 \cdot \text{H}_2\text{O}$ (5)	136
4.3	Magnetic Properties of $\text{Cl} \subset [\text{Fe}(\text{H}_2\text{L4})_3]_2(\text{OH})(\text{PF}_6)_2 \cdot \text{H}_2\text{O}$ (5)	141
4.4	Synthesis and Crystal Structure of $\text{Cl} \subset [\text{Fe}(\text{H}_2\text{L4})_3]_2(\text{FeCl}_4)_3 \cdot 2\text{C}_3\text{H}_6\text{O} \cdot 4\text{C}_7\text{H}_8$ (6)	142
4.5	Magnetic Properties of $\text{Cl} \subset [\text{Fe}(\text{H}_2\text{L4})_3]_2(\text{FeCl}_4)_3 \cdot 2\text{C}_3\text{H}_6\text{O} \cdot 4\text{C}_7\text{H}_8$ (6)	146
4.6	Synthesis and Crystal Structure of $\text{Br} \subset [\text{Fe}(\text{H}_2\text{L4})_3]_2(\text{OH})(\text{PF}_6)_2 \cdot \text{H}_2\text{O}$ (7)	147
4.7	Magnetic Properties of $\text{Br} \subset [\text{Fe}(\text{H}_2\text{L4})_3]_2(\text{OH})(\text{PF}_6)_2 \cdot \text{H}_2\text{O}$ (7)	148
4.8	Synthesis and Crystal Structure of $\text{I} \subset [\text{Fe}(\text{H}_2\text{L4})_3]_2(\text{PF}_6)_{2.23}(\text{I})_{0.21}(\text{I}_3)_{0.56} \cdot 2\text{CH}_3\text{OH}$ (8)	149
4.9	Magnetic Properties of $\text{I} \subset [\text{Fe}(\text{H}_2\text{L4})_3]_2(\text{PF}_6)_{2.23}(\text{I})_{0.21}(\text{I}_3)_{0.56} \cdot 2\text{CH}_3\text{OH}$ (8)	152
4.10	Synthesis and Crystal Structure of $\text{I} \subset [\text{Fe}(\text{H}_2\text{L4})_3]_2(\text{I})_2(\text{I}_3)_{0.6}(\text{OH})_{0.4} \cdot 0.6\text{H}_2\text{O} \cdot 2\text{CH}_3\text{OH} \cdot 2\text{C}_3\text{H}_6\text{O}$ (9)	153
4.11	Magnetic Properties of $\text{I} \subset [\text{Fe}(\text{H}_2\text{L4})_3]_2(\text{I})_2(\text{I}_3)_{0.6}(\text{OH})_{0.4} \cdot 0.6\text{H}_2\text{O} \cdot 2\text{CH}_3\text{OH} \cdot 2\text{C}_3\text{H}_6\text{O}$ (9)	154
4.12	Halide-Guest Effect on the SCO	155
4.13	Solution Studies of $\text{X} \subset$ Dimerized Helicates	156
4.14	Conclusions	164
4.15	Experimental	164
4.16	References	166

CHAPTER 4: Spin Crossover in Fe(II) Dimerized Mononuclear Triple-Stranded Helicates

4.1 Introduction

The molecular design of species incorporating the potential for host-guest interactions is an attractive approach towards the development of new SCO compounds. Taking into account this approach, Shiga et al.¹ have synthesized a dimerized Fe(II) complexes with supramolecular anion capsules. The ligand used in these complexes is a pyrazolyl-pyridine based ligand. The dimerized complexes encapsulate PF_6^- ions inside the capsule-like dimerized supramolecular structures, in which the arrangement of the bulky ligands of two intercalating discrete mononuclear complexes create a central cavity. The anionic guest interacts with ligands through hydrogen bonds with the N-H group of the pyrazole rings.

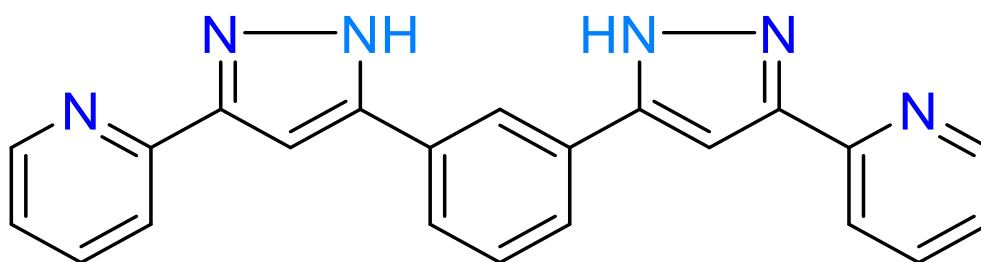


Figure 4.1: H₂L4, {1,3-bis(3-(pyridin-2-yl)-1H-pyrazol-5-yl)benzene}.

Ligand H₂L4 (Figure 4.1) was used in the previous chapter to prepare dinuclear triple stranded helicates that encapsulate halide ions. In this chapter, the change of the solvents used in the reaction yielded different supramolecular compounds using the same ligands. Dimerized mononuclear helicates $\{\text{X} \subset [\text{Fe}(\text{H}_2\text{L4})_3]_2\}^{3+}$ was prepared where a halide ion is encapsulated inside the cavity formed by the intercalating dimers. In every mononuclear helicate, one pyrazolyl-pyridine side of each ligand is not coordinated to any metal ion. The SCO behavior of the dimer is affected by the nature of the halide ions which make hydrogen bonding with the N-H groups of the pyrazole rings.

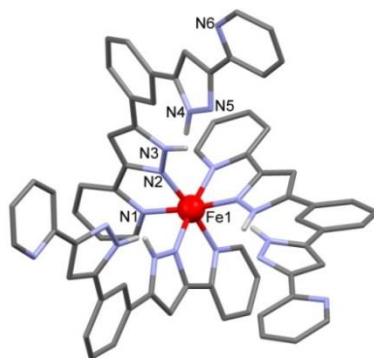


Figure 4.2: Representation of the mononuclear triple-stranded helicate $[\text{Fe}(\text{H}_2\text{L4})_3]^{2+}$ found in **5**. Encapsulated Cl^- , Counter ions and solvents are not shown. Only the hydrogen atoms on the pyrazole nitrogen atoms are shown. Gray: C and blue: N. Only Fe(II) and N atoms are labeled.

4.2 Synthesis and Crystal Structure of $\text{Cl}^-[\text{Fe}(\text{H}_2\text{L4})_3]_2(\text{OH})(\text{PF}_6)_2 \cdot \text{H}_2\text{O}$ (**5**)

The supramolecular assembly **5** was prepared by the reaction of excess of FeCl_2 with $\text{H}_2\text{L4}$ in methanol (2:3 ratio), followed by the slow diffusion of an aqueous solution of NH_4PF_6 . Thin platy crystals were obtained in low yield (12.1 %) after a few days, in addition to a fine orange solid. Despite that the iron source and the ligand are the same in the synthesis procedure of compounds **5** and **1** (see chapter 3), the differences in solvents yielded different supramolecular systems.

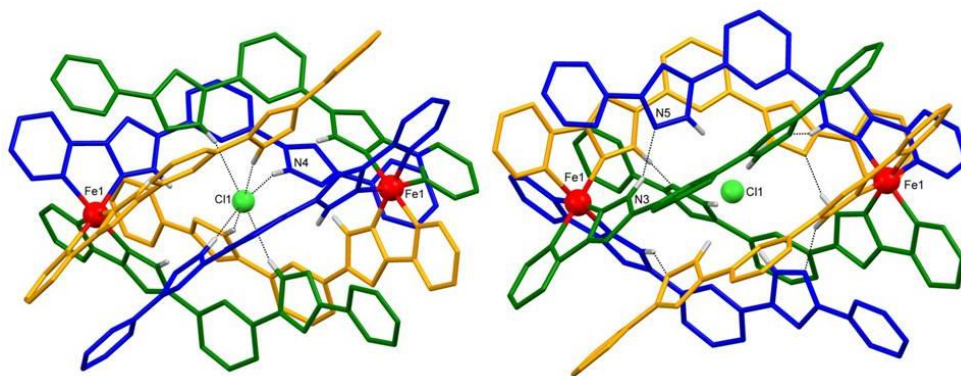


Figure 4.3: Molecular representation of $\{\text{Cl}^-[\text{Fe}(\text{H}_2\text{L4})_3]_2\}^{3+}$ cation in **5** showing the $\text{N-H}\cdots\text{Cl}^-$ hydrogen bonds with the encapsulated Cl^- ion (left), and the $\text{N-H}\cdots\text{N}\#$ hydrogen bonds between the intertwined ligands. PF_6^- and OH^- ions and H_2O molecules are omitted for clarity. Only the hydrogen atoms on the pyrazole nitrogen atoms are shown. Only metals and hetero-atoms involved in hydrogen bonding are labeled.

In spite of the poor diffraction exhibited by the crystal, the structure of **5** was unambiguously determined. The system crystallizes in the trigonal space group of $P\bar{3}c1$ where the unit cell contains two of formula assemblies. The asymmetric unit consists of one sixth of the supramolecular structure of **5**. Crystallographic data and selected structural parameters at 100 K are shown in Tables 4.1-4.2.

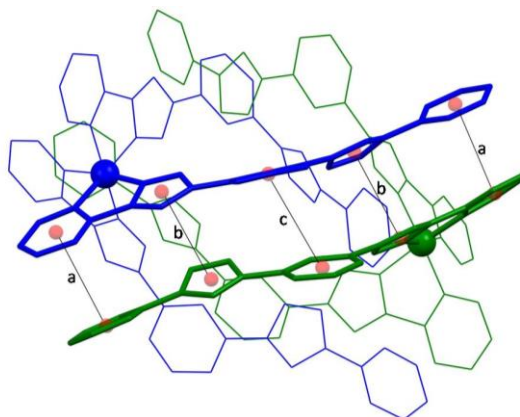


Figure 4.4: Representation of the π - π interactions between the aromatic rings of the adjacent ligands in the intertwined helicates in **5**. Centroid to centroid distances (Å) in **5/7** : (a) 3.659/3.663, (b) 3.477/3.497, (c) 3.779/3.820. (similar interactions were found in **6**, **8** and **9** with different strength over all the intertwined helicates).

The structure consists of two independent mononuclear triple-stranded helicates $[\text{Fe}(\text{H}_2\text{L4})_3]^{2+}$ (Figure 4.2) which form a dimerized assembly by encapsulation of Cl^- ion in the central cavity of the dimer (Figure 4.3) to form a $\{\text{Cl}^-[\text{Fe}(\text{H}_2\text{L4})_3]_2\}^{3+}$ cationic assembly. One OH^- and two PF_6^- anions compensate the positive charge and one water molecule is found in the lattice. In each $[\text{Fe}(\text{H}_2\text{L4})_3]^{2+}$ mononuclear helicate, three $\text{H}_2\text{L4}$ ligands offer the pseudo-octahedral environment around the Fe(II) center, each chelating with one pyrazolyl-pyridine moiety. The coordinated pyrazolyl-pyridine units are planar with torsion angle of less than 1° . These ligands adopt pseudo-S shape through twisting around the C-C bond between the central phenylene and the pyrazole groups. Moreover, the pyridine ring in the non-coordinated pyrazolyl-pyridine moiety (with twisting angle of 31.72°) displays *trans*-configuration and making hydrogen bond with the O1 (OH^- or H_2O molecules) (see below).

The two $[\text{Fe}(\text{H}_2\text{L4})_3]^{2+}$ mononuclear helicates are intertwined providing a central cavity of 30 \AA^3 (as calculated using Swiss-Pdb Viewer 4.1), which contains an encapsulated Cl^- ion. The volume of the cavity is just slightly larger than that found in the

$[\text{Cl-Fe}_2(\text{H}_2\text{L4})_3]^{3+}$ triple stranded helicate (28 \AA^3). The chloride lies on the $\text{Fe}\cdots\text{Fe}$ axis at equal distances from both metal centers ($\text{Fe1}\cdots\text{Cl1} = 5.737 \text{ \AA}$) and it is involved in strong hydrogen bonds ($\text{N4-H}\cdots\text{Cl1} = 2.534 \text{ \AA}$) with six N-H groups of the non-coordinated pyrazolyl-pyridine moieties (Figure 4.3, left). In addition, strong N-H \cdots N hydrogen bonds are present, involving the pyrazole groups of the intertwined ligands (Figure 4.3, right). Here, each N-H group close to the iron center in the mononuclear helicate makes a hydrogen bond with the closer nitrogen atom of the non-coordinated pyrazole of the other helicate [$\text{N4-H}\cdots\text{N5\#} = 1.981 \text{ \AA}$]. In addition, the adjacent ligands of the intertwined helicates are involved in five strong π - π interactions between the phenylene or pyrazole analogous aromatic rings (Figure 4.4). Three sets of such interactions are found in the dimerized helicate. All of these strong supramolecular interactions (i.e. N-H \cdots Cl and N-H \cdots N hydrogen bonds and π - π interactions) stabilize such intertwined helicates.

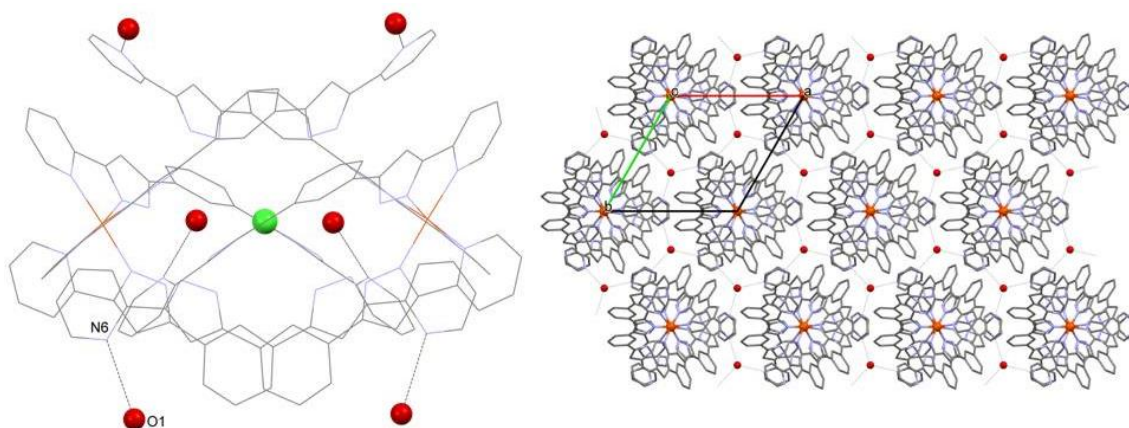


Figure 4.5: left) Representation of the six hydrogen bonds between the non-coordinated pyridine and O1 (OH^- or H_2O) in **5**. All atoms are in wireframe style except O (red) and Cl (green). Right) representation of the lattice of **5** down the crystallographic c direction, emphasizing the network resulting from the interaction of OH^- or H_2O with three neighbor helicates.

In the $[\text{FeN}_6]$ core, the $\text{Fe1-N}_{\text{pyrazole}}$ and $\text{Fe1-N}_{\text{pyridine}}$ distances are 1.928 and 1.972 \AA , respectively. This indicates a LS state of the iron centers at 100 K in agreement with bulk magnetic studies (see below). The distortion from the octahedral geometry indicated by the Σ and Θ parameters (61.77 and 199.1° , respectively) is in the range observed for LS Fe(II) centers in similar systems (see chapter 3). The intermolecular $\text{Fe1}\cdots\text{Fe1}$ distance within the dimerized helicates is 11.475 \AA which is 1.74 \AA longer

than the intrahelical Fe1...Fe2 distance (9.731 Å) observed in the $\{\text{Cl}^-[\text{Fe}_2(\text{H}_2\text{L4})_3]\}^{3+}$ dinuclear helicate (compound **1**, chapter 3).

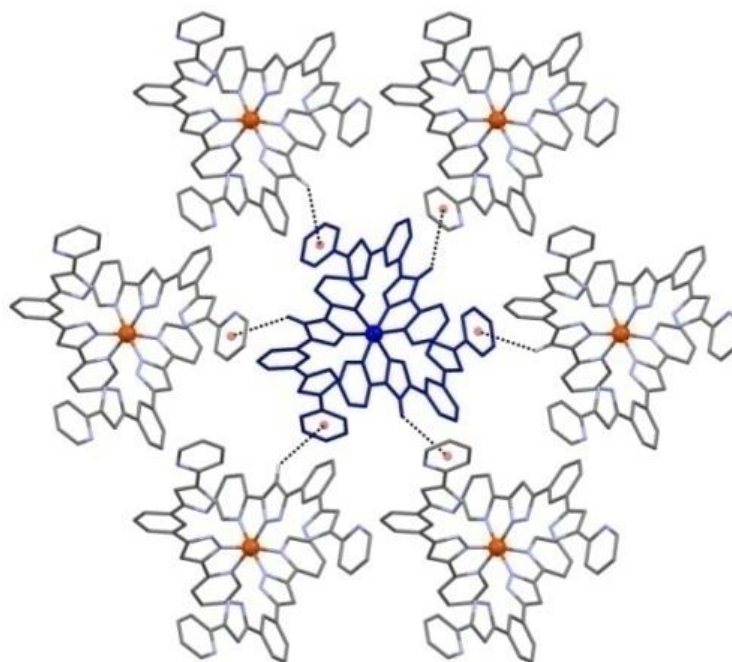


Figure 4.6: Representation of $[\text{Fe}(\text{H}_2\text{L4})_3]^{2+}$ fragment of central dimerized helicate of **5** (blue), and the surrounding equivalents first neighbors, showing the $\text{C-H}\cdots\pi$ (3.347 Å) interactions between the pyrazole and the pyridine rings.

The six non-coordinated pyridyl groups in the dimerized helicate are involved in strong hydrogen bonds ($\text{O1-H}\cdots\text{N6} = 2.047\text{Å}$) with the lattice OH^- or H_2O species (O1 in Figure 4.5). O1 is an average of the oxygen atoms belonging to the OH^- counterion and H_2O solvent molecules, which share the same position. This rationalizes the charge balance in the crystal structure and the presence of the three equal hydrogen bonds around each O1 atom with N acceptors from pyridyl groups belonging to three neighboring assemblies (N6). The organization of **5** in the lattice consists of infinite rods along the axial Fe...Fe axis of the dimerized helicate and parallel to the crystallographic *c* axis. The rods are connected to each other via strong hydrogen bonds with OH^- or H_2O molecules that fill the space between these rods together with the PF_6^- anions (Figure 4.5). The helicates of different rods are also interacting mainly *via* $\text{C-H}\cdots\pi$ (3.347 Å) interactions which involve the pyrazolyl and the pyridyl rings (Figure 4.6). The helicates within the rods are mainly involved in six $\text{C-H}\cdots\pi$ interactions between the pyridyl rings along the *c* crystallographic axis (Figure 4.7).

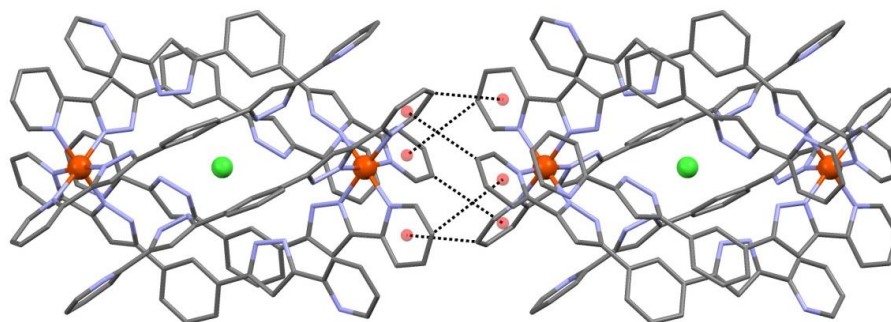


Figure 4.7: Representation of two dimerized helicates of **5** within the rod packing (see Figure 4.5), emphasizing the six intermolecular C-H \cdots π contacts linking them pairwise along crystallographic c direction. Hydrogen atoms are not shown.

Table 4.1: Crystallographic data for compound **5**, **6**, **7**, **8** and **9**

Compound	5	6	7	8	9
Formula	2(C ₆₆ H ₄₅ FeN ₁₈) 2(PF ₆), Cl, (H ₂ O), (HO)	2(C ₆₆ H ₄₈ FeN ₁₈) Cl, 3(Cl ₄ Fe), 4(C ₇ H ₈), 2(C ₃ H ₆ O)	2(C ₆₆ H ₄₅ FeN ₁₈) 2(PF ₆), Br, (H ₂ O), (HO)	2(C ₆₆ H ₄₈ FeN ₁₈) 2.23(PF ₆), 1.21(I), 0.56(I ₃), 2(CH ₄ O)	2(C ₆₆ H ₄₈ FeN ₁₈) 2(C ₃ H ₆ O), 3I, 0.6(I ₃), 0.8(H O), 1.2(H ₂ O)
Mr	2652.51	3411.23	2703.02	3051.93	3126.77
Wavelength	0.77490	0.7728	0.77490	0.77490	0.77490
T (K)	100	100	100	100	100
Crystal system	Trigonal	Triclinic	Trigonal	Monoclinic	Monoclinic
Space group	<i>P</i> -3 <i>CI</i>	<i>P</i> -1	<i>P</i> -3 <i>CI</i>	<i>P</i> 2 ₁ / <i>n</i>	<i>C</i> 2/ <i>c</i>
<i>Z</i>	2	2	2	4	4
<i>a</i> [Å]	13.4555(8)	13.4928(6)	13.5619(5)	24.356(1)	23.9867(8)
<i>b</i> [Å]	13.4555(8)	21.3643(10)	13.5619(5)	13.6794(7)	13.4513(5)
<i>c</i> [Å]	37.438(3)	28.7728(13)	37.307(2)	39.437(2)	40.6047(14)
α [°]	90	73.320(3)	90	90	90
β [°]	90	80.537(3)	90	97.682(3)	91.448(2)
γ [°]	120	85.230(3)	120	90	90
<i>V</i> [Å ³]	5870.1(8)	7831.4(6)	5942.4(5)	13021.5(11)	13097.0(8)
ρ_{calc} (gcm ⁻³)	1.501	1.447	1.511	1.557	1.586
μ (mm ⁻¹)	0.487	0.933	0.867	1.274	1.778
Independent reflections	1230	34424	4960	18863	13380
Restraints/parameters	269/285	434/2057	1/285	536/1861	40/889
Goodness of fit on F ²	1.098	1.052	1.150	1.060	1.099
Final R ₁ /wR ₂	0.1400/	0.0805/	0.0651/	0.1231/	0.0844/
[I>2 σ (I)]	0.3012	0.1812	0.1644	0.3389	0.2120
Final R ₁ /wR ₂	0.1594/	0.1300/	0.0764/	0.1547/	0.1096/
[all data]	0.3138	0.1812	0.1725	0.3705	0.2253
Largest diff. peak and hole	0.664/	1.176/	1.416/	2.747/	1.387/
(eÅ ⁻³)	-0.366	-1.339	-1.090	-3.424	-3.425

Table 4.2: Selected bond and interatomic distances [\AA] and structural parameters found in **5** and **7**.

Compound	5	7
Fe1-N1	1.97	1.993
Fe1-N2	1.93	1.945
Fe1...Fe1#	11.475	11.388
Fe1...X1	5.737	5.6938
N4-H...X1	2.5338	2.6033
N3-H...N5#	1.98	2.009
O1-H...N6	2.0(4)	2.09(5)
(Fe-N) _{avg}	1.950	1.969
$\Sigma \angle$	61.77	63.84
$\Theta \angle$	199.1	201.3
$V_{oct} (\text{\AA}^3)$	9.72	10.00

4.3 Magnetic Properties of $\text{Cl} \left[\text{Fe}(\text{H}_2\text{L4})_3 \right]_2 (\text{OH})(\text{PF}_6)_2 \cdot \text{H}_2\text{O}$ (**5**)

Magnetic susceptibility measurements were carried out on a crystalline sample of **5** in the temperature range 2-395K, using a constant magnetic field of 0.5 T. The thermal variation of the magnetic susceptibility by the temperature product ($\chi_M T$) in the heating and cooling modes is represented in Figure 4.8.

Upon heating, the $\chi_M T$ value below 300 K indicates a LS state for the Fe(II) centers with the existence of some residual HS centers. The $\chi_M T$ value of around $0.17 \text{ cm}^3 \text{ mol}^{-1} \text{ K}$ in the low temperatures range corresponds to ca. 2.8 % of HS residual Fe(II) centers. This agrees with the crystal structure at 100 K, which shows two LS Fe(II) centers. The jump in the $\chi_M T$ value in the temperature range 50-100 K mostly corresponds to the accidental presence of some oxygen during the measurements. Below 10 K, a slight decrease in $\chi_M T$ to reach $0.10 \text{ cm}^3 \text{ mol}^{-1} \text{ K}$ is due to zero field splitting (ZFS) of the residual HS centers.

Above 310 K, a gradual increase in $\chi_M T$ value was observed up to $1.9 \text{ cm}^3 \text{ mol}^{-1} \text{ K}$ at the maximum value of temperature measured, 395 K. This value corresponds to a LS \rightarrow HS conversion of ca. 30 % of the Fe(II) centers. This increase indicates a gradual SCO behavior which is not complete up to the maximum temperature limit of the SQUID magnetometer.

In the cooling sweep, a significant difference in the magnetic behavior was observed. Below 395 K, the $\chi_M T$ value decreased in a more gradual fashion down to 180 K with $\chi_M T = 0.45 \text{ cm}^3 \text{ mol}^{-1} \text{ K}$. The SCO process in the cooling mode occurs over a larger temperature range than the heating mode, by approximately 120 K. The loss of some lattice solvent molecules at high temperatures is probably the reason of such change in the magnetic response between the heating and the cooling sweeps. The plateau in the range 80-180 K indicates a residual HS centers of ca. 7 % ($\chi_M T = 0.42 \text{ cm}^3 \text{ mol}^{-1} \text{ K}$).

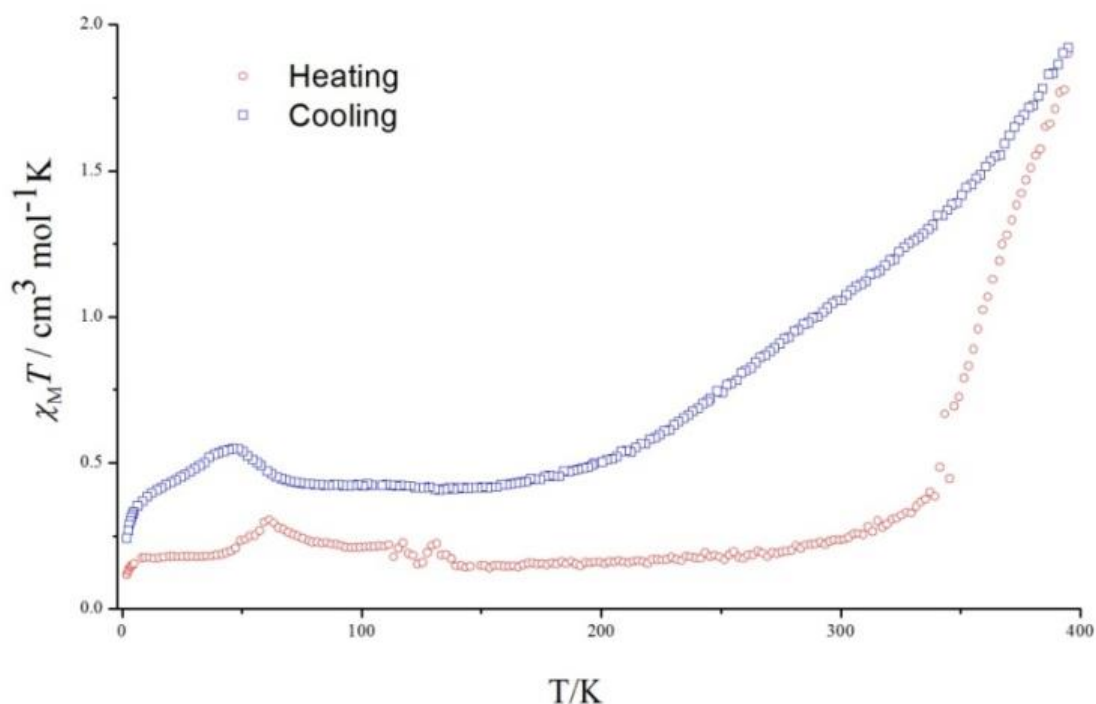


Figure 4.8: Variable temperatures magnetic susceptibility measurements for **5** measured in 0.5 T *dc* magnetic field.

4.4 Synthesis and Crystal Structure of $\text{Cl}[\text{Fe}(\text{H}_2\text{L4})_3]_2(\text{FeCl}_4)_3 \cdot 2\text{C}_3\text{H}_6\text{O} \cdot 4\text{C}_7\text{H}_8$ (**6**)

The preparation of **6** was conducted in acetone by mixing the iron source (FeCl_2) with the ligand ($\text{H}_2\text{L4}$) in the 1:1 molar ratio. Slow diffusion of toluene to the resulting solution yielded red crystals. The oxidation of part of Fe(II) in the presence of excess chloride ions have led to the formation of $[\text{FeCl}_4]^-$ which is not rare and has been seen in similar systems.¹

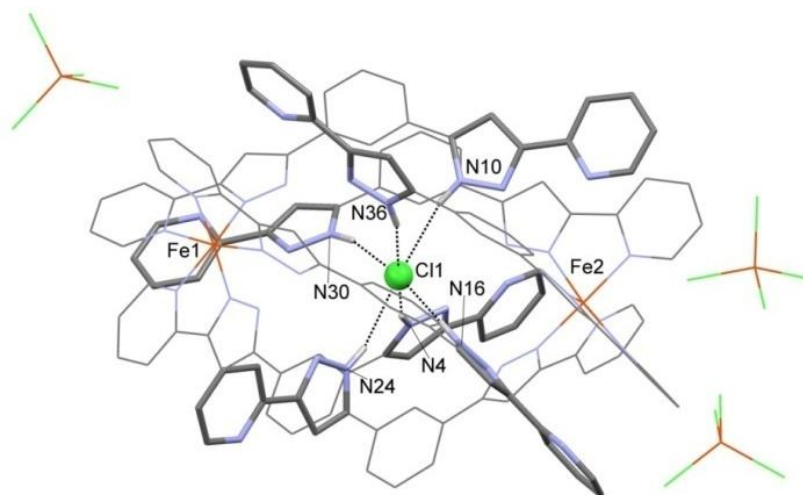


Figure 4.9: Molecular representation of $\text{Cl}^-[\text{Fe}(\text{H}_2\text{L}_4)_3]_2(\text{FeCl}_4)_3$ (**6**), showing the $\text{N}-\text{H}\cdots\text{Cl}$ interactions and emphasizing the *cis*- or *trans*- configuration of the non-coordinated pyridine rings. All the structure shown in wireframe style except the non-coordinated pyrazolyl-pyridine moiety (capped-sticks) and the Cl^- ion (ball). Only the H atoms involved in hydrogen bonding with Cl^- are shown. Only selected atoms are labeled.

Compound **6** crystallizes in the triclinic space group *P*-1, where the asymmetric unit consists of the cationic dimerized helicate $\{\text{Cl}^-[\text{Fe}(\text{H}_2\text{L}_4)_3]_2\}^{3+}$ and three FeCl_4^- ions in addition to two and four solvent molecules of acetone and toluene, respectively. The unit cell contains two such assemblies. Crystallographic data and selected structural parameters at 100 K are shown in Table 4.3. The Cl-encapsulated dimer $\{\text{Cl}^-[\text{Fe}(\text{H}_2\text{L}_4)_3]_2\}^{3+}$ seen here is similar to the one observed in **5**. However, there are some differences manifested as two crystallographic unique iron centers and the presence of a different configuration (i.e. *cis*- and *trans*-) of the non-coordinated pyridine. Both iron centers exhibit the LS state at 100 K as indicated by the Fe-N distances and the octahedral distortion around the Fe(II) centers [$(\text{Fe}-\text{N})_{\text{avg}} = 1.986, 1.980\text{\AA}$; $\Sigma = 59.61, 59.81^\circ$; $\Theta = 181.2, 185.2^\circ$ for Fe1 and Fe2, respectively] in agreement with the magnetic studies (see below). Free-of-coordination pyridine rings exhibit the *cis*- configuration in half of the ligands and *trans*- configuration in the rest of them (Figure 4.9). In the former, the pyridine rings are interacting through $[\text{N}_{\text{pyridine}}\cdots\text{H}-\text{N}_{\text{pyrazole}}]$ hydrogen bonds with the closet ligand and through $[\text{C}-\text{H}\cdots\text{Cl}]$ or $[\text{C}-\text{H}\cdots\text{O}]$ ($\text{C}-\text{H}$ in the *ortho* position) with FeCl_4^- or acetone molecules (Figure 4.10). These interactions are the responsible of stabilization of the less favored *cis*- configuration in these three ligands. The π - π interactions between the intertwined ligands are similar to

these shown in Figure 4.4 for **5**. However, the strength of these interactions is different through all the dimerized helicate and the centroid to centroid distances fall in the 3.517-3.977 Å range. In addition, the N-H...Cl [2.509-2.596 Å] and the N-H...N_{pyrazole} [1.999-2.056 Å] through the {Cl₂[Fe(H₂L4)₃]₂}³⁺ moiety here exhibit different strength as consequence of the asymmetric nature of the two mononuclear helicates and the non-centered position of the Cl⁻ ion [Fe1...Cl1 = 5.863, Fe1...Cl1 = 5.843 Å].

The packing of the lattice in **6** consists of infinite rods along the Fe...Fe helical axis and slightly shifted along the *b* axis (Figure 4.11). The spaces between these rods are filled with FeCl₄⁻, acetone and toluene molecules. The helicates in the different rods are interacting through C-H...Cl [2.712-2.765 Å] and C-H...π [2.752-2.769 Å] non-classical hydrogen bonds with FeCl₄⁻ counterions or toluene solvent molecules, respectively (Figure 4.12).

Table 4.3: Selected bond and interatomic distances [Å] and structural parameters found in **6**.

Fe1-N1	1.998(4)	Fe2-N21	1.994(5)
Fe1-N2	1.960(4)	Fe2-N22	1.967(4)
Fe1-N7	2.016(4)	Fe2-N27	2.002(4)
Fe1-N8	1.968(4)	Fe2-N28	1.958(4)
Fe1-N13	2.008(5)	Fe2-N33	2.002(4)
Fe1-N14	1.963(4)	Fe2-N34	1.958(5)
Fe1...Fe2	11.706(1)	Fe2...Cl1	5.843(2)
Fe1...Cl1	5.863(2)	N4-H...Cl1	2.503
N10-H...Cl1	2.569	N24-H...Cl1	2.509
N16-H...Cl1	2.552	N30-H...Cl1	2.593
N36-H...Cl1	2.529	N9-H...N37	2.018
N15-H...N25	2.052	N23-H...N17	2.055
N3-H...N31	2.056	N9-H...N38	2.924
N29-H...N5	1.999	N29-H...N6	2.911
N35-H...N11	2.007	N35-H...N12	2.999
(Fe-N) _{avg} ^a	1.986/1.980	Σ∠ ^a	59.61/59.81
∠ ^a	181.2/185.2	V _{oct} (Å ³) ^a	10.28/10.19
a: In Fe1/Fe2 form			

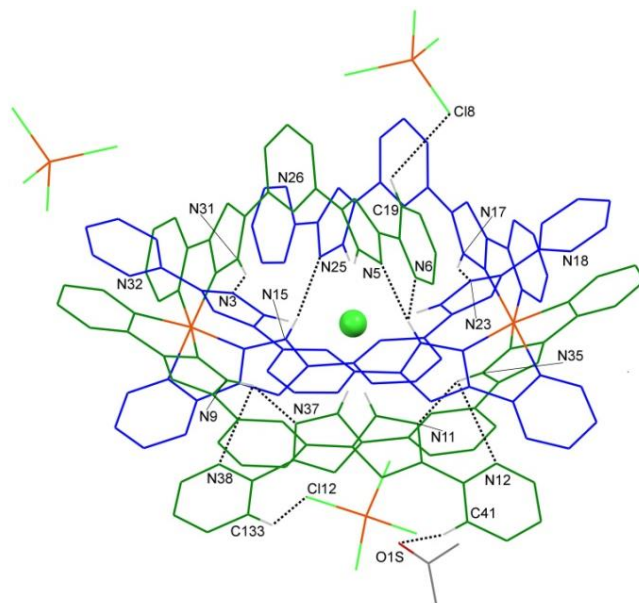


Figure 4.10: Molecular representation of **6** showing: the $\text{N-H}\cdots\text{N}_{\text{pyrazole}}$, $\text{N-H}\cdots\text{N}_{\text{pyridine}}$, $\text{C-H}\cdots\text{O}$ and $\text{C-H}\cdots\text{Cl}$ hydrogen bonds. The ligands with *cis*- and *trans*- non-coordinated pyridine rings are shown in green and blue, respectively. In the former the *ortho* C-H groups are interacting with FeCl_4^- or acetone species and the $\text{N}_{\text{pyridine}}$ atom is also interacting with the NH group of the closet pyrazole which force this configuration. One acetone and four toluene molecules are omitted for clarity. Only selected hydrogen atoms are shown and only selected atoms are labeled.

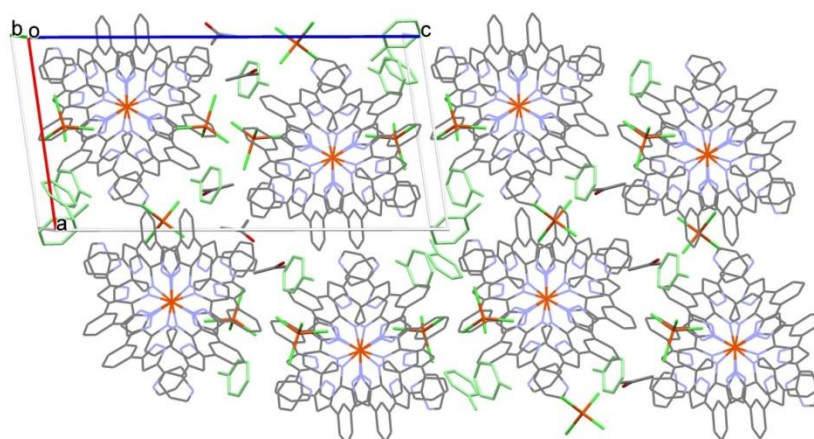


Figure 4.11: Representation of the lattice packing in **6** as rods of the $\{\text{Cl}[\text{Fe}(\text{H}_2\text{L}_4)_3]_2\}^{3+}$ helicates slightly shifted along the *b* axis and separated by FeCl_4^- , toluene and acetone molecules.

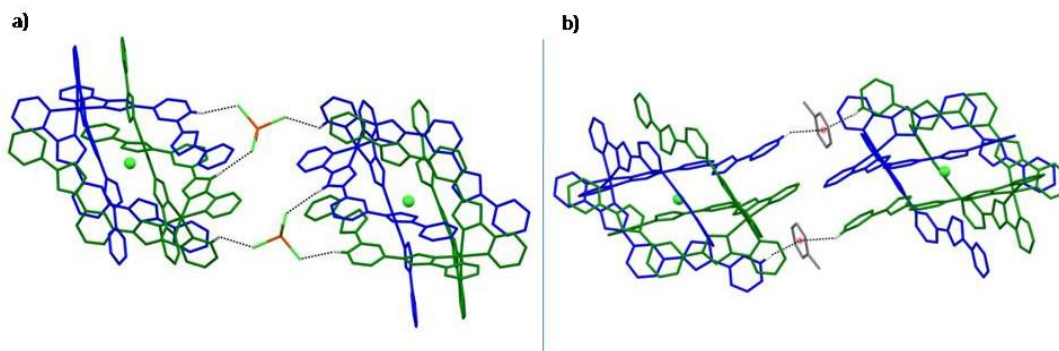


Figure 4.12: Representation of the C-H...Cl [2.712-2.765 Å] (a) and the C-H... π [2.752-2.769 Å] (b) interactions between the dimerized helicates in **6**. These interactions involve helicates belong to different rod (see Figure 4.11) and FeCl_4^- or toluene molecules. The dimerized helicate shown in blue and green. Only the hydrogen atoms involved in the interactions are shown in white.

4.5 Magnetic Properties of $\text{Cl} \left[\text{Fe}(\text{H}_2\text{L4})_3 \right]_2 (\text{FeCl}_4)_3 \cdot 2\text{C}_3\text{H}_6\text{O} \cdot 4\text{C}_7\text{H}_8$ (**6**)

Magnetic susceptibility measurements of **6** were performed on a crystalline sample in the temperature range 2-397 K, using a constant magnetic field of 0.5 T. The data are represented as $\chi_M T$ vs. T plots in the heating and cooling modes in Figure 4.13.

In the heating sweep, the $\chi_M T$ value at 60 K was $14.80 \text{ cm}^3 \text{ mol}^{-1} \text{ K}$, which corresponds to the value expected for three isolated HS Fe(III) ions with ($g = 2.12$, $S = 5/2$). This agrees well with the crystal structure which shows three FeCl_4^- counterions and two Fe(II) centers in the LS state at 100 K. Above 250 K, a gradual increase in $\chi_M T$ value was detected as a consequence of incomplete SCO, up to 397 K. The maximum $\chi_M T$ value of $20.93 \text{ cm}^3 \text{ mol}^{-1} \text{ K}$ at the upper temperature limit of the SQUID magnetometer corresponds to *ca.* 82% of LS \rightarrow HS conversion of the Fe(II) centers. The sharp decline in $\chi_M T$ below 50 K down to $9.43 \text{ cm}^3 \text{ mol}^{-1} \text{ K}$ is due to zero field splitting (ZFS) of the HS Fe(III) centers. The SCO behavior now is more gradual and shifted to lower temperature compared to the one seen in **5**.

Upon cooling from 397 K down to 55 K, a continuous decrease in $\chi_M T$ value was observed from $20.93 \text{ cm}^3 \text{ mol}^{-1} \text{ K}$ to $14.43 \text{ cm}^3 \text{ mol}^{-1} \text{ K}$. This magnetic response is different from the one seen in the heating mode; the SCO occurs in a more gradual manner over a wide temperature range of 340 K and also, it is shifted to lower temperatures compared with the one seen in the heating mode. This behavior is similar

to that seen in **5**, which is probably due to losing some lattice solvents at high temperatures.

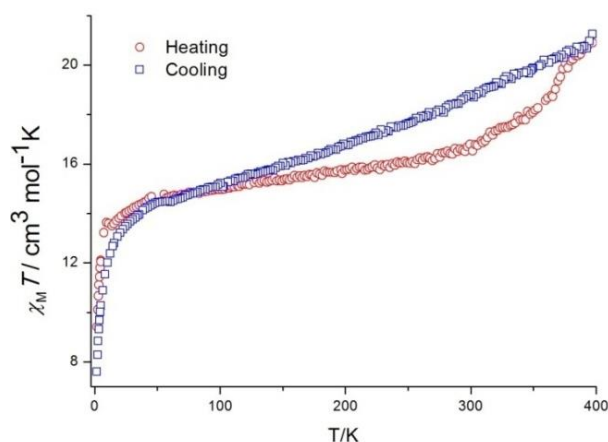


Figure 4.13: Variable temperatures magnetic susceptibility measurements for **6** measured in 0.5 T *dc* magnetic field.

4.6 Synthesis and Crystal Structure of $\text{Br}^-\text{[Fe(H}_2\text{L4)}_3\text{]}_2(\text{OH})(\text{PF}_6)_2 \cdot \text{H}_2\text{O}$ (**7**)

The preparation procedure of **7** is the same as in **5**, except using now FeBr_2 as iron source. The resulting compound is isostructural with **5**, the only significant difference being that the encapsulated anion is now a Br^- ion (Figure 4.14). Crystallographic data and selected structural parameters at 100 K are shown in Table 4.2.

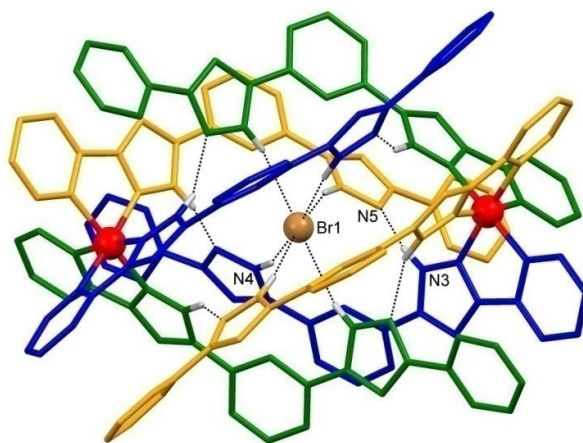


Figure 4.14: Molecular representation of $\{\text{Br}^-\text{[Fe(H}_2\text{L4)}_3\text{]}_2\}^{3+}$ cation in **7** showing the N-H \cdots Cl hydrogen bonds with the encapsulated Cl^- ion and the N-H \cdots N# hydrogen bonds between the intertwined ligands. PF_6^- , OH^- anions and H_2O molecules are omitted for clarity.

Only the hydrogen atoms on the pyrazole nitrogen atoms are shown. Only hetero-atoms involved in hydrogen bonding are labeled.

The hydrogen bonds and the π - π interactions here show larger distances than in the Cl⁻ analogue [N4-H \cdots Br1 = 2.603, N3-H \cdots N5# = 2.069, O1-H \cdots 2.087 Å] (Table 4.2, Figures 4.14 and 4.4). Although the intra-dimer Fe1 \cdots Fe1# distance [11.388 Å] here is shorter than that observed in **5** by 0.087 Å, the volume of the cavity is larger [35 Å³], in order to accommodate better the Br⁻ ion. As in **5**, the state of the Fe(II) centers is LS at 100 K, as indicated by the (Fe-N)_{avg} distances and the octahedral distortion parameters [(Fe-N)_{avg} = 1.969 Å, Σ = 63.84°, Θ = 201.3°]. However, the structural and chemical differences yielded a different magnetic behavior at high temperatures as shown by bulk magnetic studies (see section 4.12). The lattice packing is similar to that seen for the Cl⁻ analogue (Figures 4.5 and 4.6).

4.7 Magnetic Properties of Br⁻[Fe(H₂L4)₃]₂(OH)(PF₆)₂·H₂O (**7**)

Magnetic susceptibility measurements of **7** were performed on a crystalline sample in the temperature range 5-397 K, using a constant magnetic field of 0.5 T. The data are represented as $\chi_M T$ vs. T plots in the heating and cooling modes in Figure 4.15.

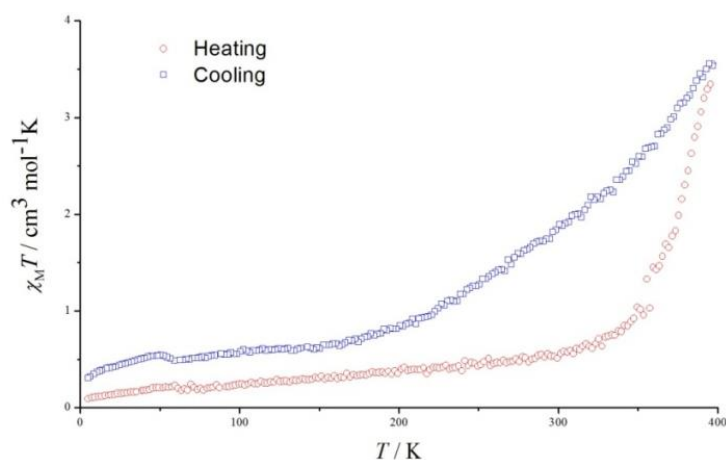


Figure 4.15: Variable temperatures magnetic susceptibility measurements for **7** measured in 0.5 T *dc* magnetic field.

During the heating mode, the $\chi_M T$ value increases slightly in the temperature range 5-300 K from 0.092 to 0.54 cm³ mol⁻¹ K. These $\chi_M T$ values at low temperatures indicate LS state for both Fe(II) ions, with residual HS centers of *ca.* 2 %, in agreement with the crystal structure at 100 K, which shows LS Fe(II) centers. A gradual SCO behavior was observed starting from 300 K up to 397 K, with a maximum $\chi_M T$ value of 3.56 cm³ mol⁻¹ K. This correspond to a LS \rightarrow HS SCO of *ca.* 60 % of both Fe(II) centers ($\chi_M T$ = 6.00

$\text{cm}^3\text{mol}^{-1}\text{K}$ for two Fe(II) ions, $g = 2.00$ and $S = 2$). Similar to the previous dimerized helicates, this gradual SCO behavior is not complete at the maximum temperature limit of the SQUID magnetometer and shows a distinct behavior in the cooling mode probably due to losing some lattice solvents.

4.8 Synthesis and Crystal Structure of

$\text{I} \cdot [\text{Fe}(\text{H}_2\text{L4})_3]_2(\text{PF}_6)_{2.23}(\text{I})_{0.21}(\text{I}_3)_{0.56} \cdot 2\text{CH}_3\text{OH}$ (**8**)

Compound **8** was prepared by the reaction of excess FeI_2 with $\text{H}_2\text{L4}$ in methanol, followed by the addition of NH_4PF_6 . Red crystals were obtained after leaving the resulting solution for slow evaporation. It was shown in a different section that the dinuclear triple stranded helicate assembly $[\text{Fe}_2(\text{H}_2\text{L4})_3]^{3+}$ could not encapsulate the big halide I^- (chapter 3) as a result of the limited space of the central cavity. In contrast, the dimerized mononuclear triple stranded helicate here can encapsulate I^- thanks to the flexibility of the assembly.

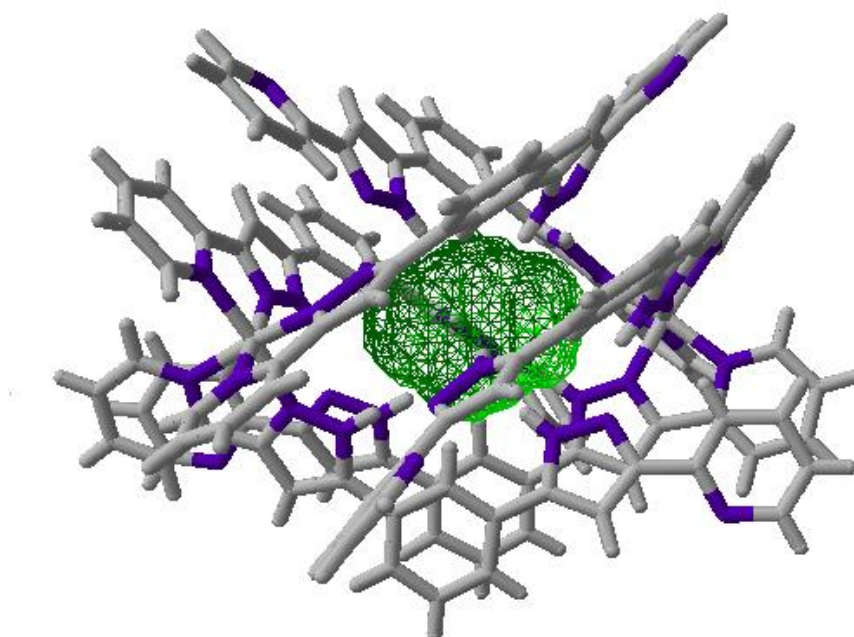


Figure 4.16: Representation of the $[\text{Fe}(\text{H}_2\text{L4})_3]_2^{4+}$ host helicate of **8** (encapsulated I^-) with the anions removed and the volume of the central cavity highlighted as green surface using Swiss-Pdb viewer 4.1 (cavity volume = 48 \AA^3).

The volume inside the $[\text{Fe}(\text{H}_2\text{L4})_3]_2^{4+}$ host was calculated from the molecular structure of **5** (Cl^-), **7** (Br^-) and **8** (I^-) as 30, 35 and 48 \AA^3 , respectively, using Swiss-Pdb viewer 4.1 (Figure 4.16). The packing coefficient ($\text{PC} = V_{\text{guest}}/V_{\text{cavity}}$, see chapter 3) for Cl^- , Br^- , and

Γ in **5**, **7** and **8** was calculated to be 0.650, 0.729 and 0.814, respectively. These values are expected for such systems with a lot of strong hydrogen bonds². The absence of coordination bonds between the dimerized helicates in $[\text{Fe}(\text{H}_2\text{L4})_3]_2^{4+}$ give the necessarily flexibility to accommodate the big Γ ion.

Compound **8** crystallizes in the monoclinic space group $P2_1/n$ ($Z = 4$). Crystallographic data and structural parameters at 100 K are shown in Table 4.4. The asymmetric unit consists of the cationic dimerized helicate $\{\text{I} \subset [\text{Fe}(\text{H}_2\text{L4})_3]_2\}^{3+}$ where the tri-positive charge is compensated by: PF_6^- and tri-iodide I_3^- ions, which are disordered over three positions with total occupancy of 2.21 and 0.56, respectively, and an Γ ion, with 0.21 occupancy. The dimerized helicate $\{\text{I} \subset [\text{Fe}(\text{H}_2\text{L4})_3]_2\}^{3+}$ is similar to that seen for Cl^- (**5**) and Br^- (**7**). However, the two iron centers here are crystallographically unique and the Γ ion is located closer to Fe1 by 0.081 Å [$\text{Fe1} \cdots \text{I1} = 5.709$ and $\text{Fe2} \cdots \text{I1} = 5.790$ Å]. The $(\text{Fe-N})_{\text{avg}}$ distances and the octahedral distortion parameters indicate two LS iron centers at 100 K [$(\text{Fe-N})_{\text{avg}} = 1.968, 1.971$ Å; $\Sigma = 65.08, 58.01^\circ$; $\Theta = 200.1, 184.2^\circ$ for Fe1 and Fe2 respectively]. $\text{N-H} \cdots \text{I}$ and $\text{N-H} \cdots \text{N}$ interactions here are weaker than that seen in **5** and **7** (Figure 4.17 and Table 4.4). This difference in nature of the halide and therefore the strength of the interactions affects the spin transition temperature (see below).

The disordered PF_6^- ions are sharing their space with the disordered I_3^- species and the outer Γ ions, which occupy the voids left in their absence. These ions do not interact significantly with the helicates. In contrast, one methanol molecule interacts with one non-coordinated pyridine [$\text{O15-H} \cdots \text{N26} = 2.107$ Å] and the other methanol interacts with the former methanol molecule [$\text{O2S-H} \cdots \text{O1S} = 2.112$ Å] (Figure 4.17). The π - π interactions between the intertwined ligands are similar to these shown in Figure 4.4 for **5**. However, the strength of these interactions is different through all the dimerized helicate and the centroid to centroid distances fall in the 3.515-4.051 Å range. The organization of **8** in the lattice is different than the previous dimerized helicates. The packing consist of alternative layers of the hydrophobic $\{\text{I} \subset [\text{Fe}(\text{H}_2\text{L4})_3]_2\}^{3+}$ sheets and the hydrophilic counterions in the ac plane (Figure 4.18). The helicates interact within the sheets via π - π and $\text{C-H} \cdots \pi$ interactions of the numerous phenyl groups (Figure 4.18).

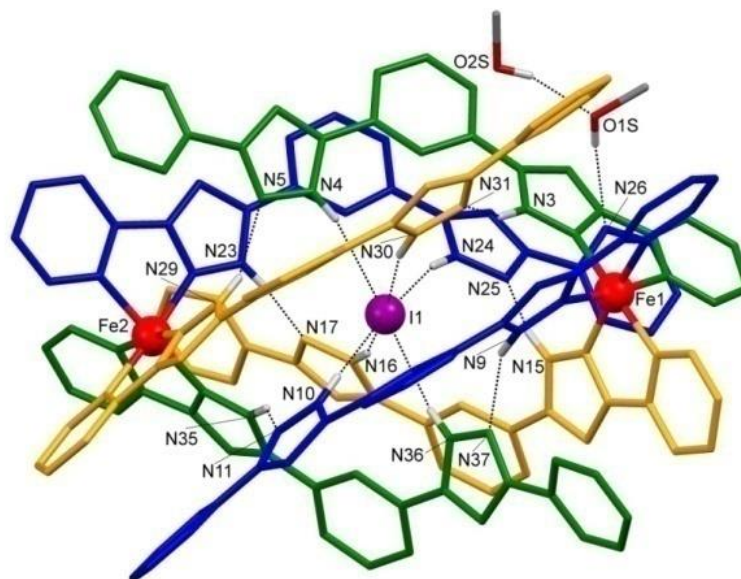


Figure 4.17: Molecular representation of $\{\text{Ic}[\text{Fe}(\text{H}_2\text{L}_4)_3]_2\}^{3+}$ cation in **8** showing the N-H \cdots I hydrogen bonds with the encapsulated I $^-$ ion, the N-H \cdots N hydrogen bonds between the intertwined ligands and the interaction with CH $_3$ OH solvent molecules. PF $_6^-$ and I $_3^-$ and I $^-$ ions are omitted for clarity. Only the hydrogen atoms on the pyrazole nitrogen atoms are shown. Only hetero-atoms involved in hydrogen bonding are labeled. The three ligands shown in different colors.

Table 4.4: Selected bond and interatomic distances [\AA] and structural parameters found in **8**.

Fe1-N1	1.975(8)	Fe2-N21	2.00(1)
Fe1-N2	1.953(8)	Fe2-N22	1.949(8)
Fe1-N7	1.978(9)	Fe2-N27	2.003(8)
Fe1-N8	1.947(8)	Fe2-N28	1.937(8)
Fe1-N13	2.00(1)	Fe2-N33	1.972(9)
Fe1-N14	1.960(8)	Fe2-N34	1.963(8)
Fe1 \cdots Fe2	11.498(2)	Fe2 \cdots I1	5.790(2)
Fe1 \cdots I1	5.709(2)	N4-H \cdots I1	2.654
N10-H \cdots I1	2.6608	N24-H \cdots I1	2.6713
N16-H \cdots I1	2.6282	N30-H \cdots I1	2.6381
N36-H \cdots I1	2.629	N9-H \cdots N37	2.072
N15-H \cdots N25	2.063	N23-H \cdots N17	2.044
N3-H \cdots N31	2.029	N29-H \cdots N5	2.07
N11-H \cdots N35	2.03	O1S-H \cdots N26	2.11
O2S-H \cdots O1S	2.11		
(Fe-N) $_{\text{avg}}$ ^a	1.968/1.971	$\Sigma \angle$ ^a	65.08/58.01
Θ ^a	200.2/184.1	$V_{\text{oct}} (\text{\AA}^3)$ ^a	9.98/10.04

a: In Fe1/Fe2 form

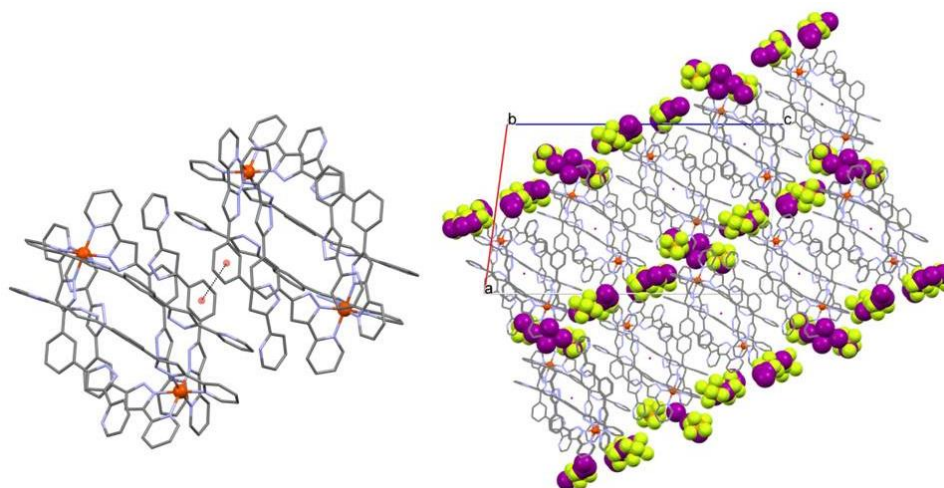


Figure 4.18: Representation of the packing in **8** consisting of alternative layers of the $\{\text{I}[\text{Fe}(\text{H}_2\text{L4})_3]_2\}^{3+}$ helicite sheets and the counterions (right). The helicites interact via π - π and $\text{C-H}\cdots\pi$ interactions (left, only π - π interactions are shown). The counterions shown in spacefill style except the encapsulated I^- which shown in wireframe style. The iron atoms shown as orange balls. Methanol molecules were deleted for clarity.

4.9 Magnetic Properties of $\text{I}[\text{Fe}(\text{H}_2\text{L4})_3]_2(\text{PF}_6)_{2.23}(\text{I})_{0.21}(\text{I}_3)_{0.56}\cdot 2\text{CH}_3\text{OH}$ (**8**)

Magnetic susceptibility measurements of **8** were carried out on a crystalline sample in the temperature range 5-397 K, using a constant magnetic field of 0.5 T. Figure 4.19 represents the data as $\chi_M T$ vs. T plots in the heating and cooling sweeps.

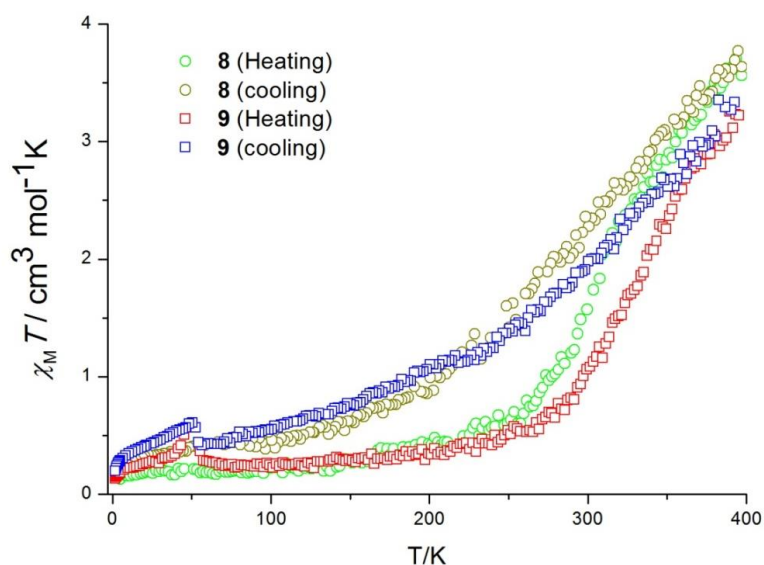


Figure 4.19: Variable temperatures magnetic susceptibility measurements for **8** and **9** measured in 0.5 T *dc* magnetic field.

Upon heating from 5–200 K, a plateau was observed with $\chi_M T$ around $0.23 \text{ cm}^3 \text{ mol}^{-1} \text{ K}$ indicating a low spin state for both Fe(II) centers with less than 4% of residual HS centers. This agrees with the crystal structure at 100 K. Starting from 200 K, a gradual increase in the $\chi_M T$ value was observed to reach a maximum value of $3.70 \text{ cm}^3 \text{ mol}^{-1} \text{ K}$ at 395 K. This value corresponds to 62% of LS \rightarrow HS conversion of the Fe(II) centers. The gradual SCO process is not complete at the temperature range available in the SQUID magnetometer, and it is expected to continue above 400 K. During the cooling process, the $\chi_M T$ vs. T curve exhibits a different behavior as seen for the previous compounds.

4.10 Synthesis and Crystal Structure of

$\text{I} \subset [\text{Fe}(\text{H}_2\text{L4})_3]_2(\text{I})_2(\text{I3})_{0.6}(\text{OH})_{0.4} \cdot 0.6\text{H}_2\text{O} \cdot 2\text{CH}_3\text{OH} \cdot 2\text{C}_3\text{H}_6\text{O}$ (9)

Compound **9** was prepared by the reaction of $\text{Fe}(\text{CF}_3\text{SO}_3)_2$ with $\text{H}_2\text{L4}$ in methanol followed by the addition of excess Bu_4NI , which yielded a red precipitate which was re-dissolved in nitromethane. Red crystals were obtained after two weeks by slow vapor diffusion of ethylacetate to the latter solution. Two acetone molecules were found in the lattice which could be due to some traces of acetone in the solvents.

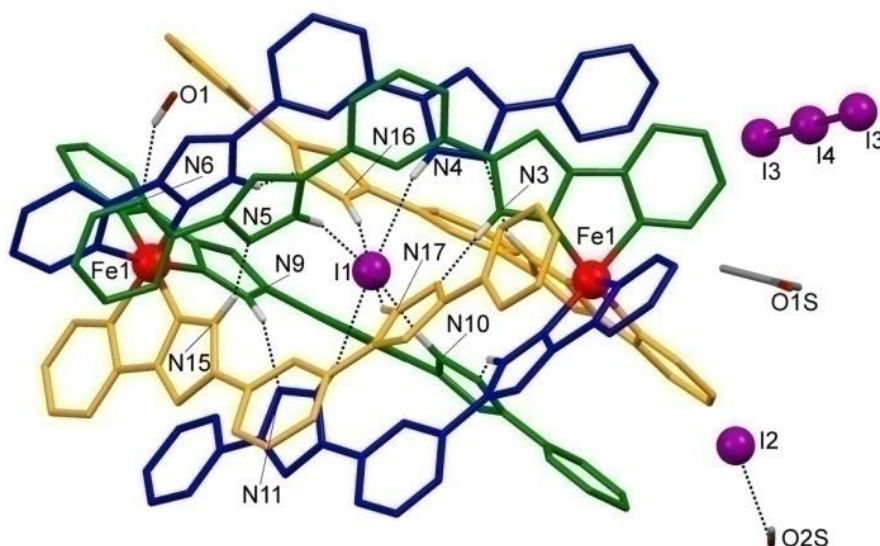


Figure 4.20: Representation of the molecular structure in **9** showing the N–H \cdots I hydrogen bonds with the encapsulated I $^-$ ion, the N–H \cdots N hydrogen bonds between the intertwined ligands and the interaction with OH $^-$. One outer I $^-$ and one acetone and one methanol molecules are omitted for clarity. Only the hydrogen atoms on the pyrazole nitrogen atoms are shown.

Only hetero-atoms involved in hydrogen bonding are labeled.

Table 4.5: Selected bond and interatomic distances [\AA] and structural parameters found in **9**.

Fe1-N1	1.997(6)	Fe1-N8	1.949(5)
Fe1-N2	1.961(7)	Fe1-N13	1.994(6)
Fe1-N7	1.982(7)	Fe1-N14	1.948(5)
Fe1...Fe1#	11.464(1)	Fe1...I1	5.7321
N4-H...I1	2.6493	N15-H...N5#	2.074
N10-H...I1	2.6234	N3-H...N17#	2.045
N16-H...I1	2.6321	N9-H...N11#	2.033
O1-H1...N6	2.104	O1-H2...N12	2.229
O1-H3...N18	2.207		
(Fe1-N) _{avg}	1.972	$\Sigma \angle$	57.96
$\theta(\angle)$	183.2	$V_{oct}(\text{\AA}^3)$	10.06

Compounds **9** crystallizes in the monoclinic space group $C2/c$ with $Z = 4$. Crystallographic data and structural parameters at 100 K are shown in Table 4.5. The structure consists of the dimerized helicate $\{\text{I}[\text{Fe}(\text{H}_2\text{L4})_3]_2\}^{3+}$, two I^- ions, a tri-iodide I_3^- ion with 0.6 occupancy, an OH^- ion with 0.4 occupancy, a water molecule with 0.6 occupancy, two lattice molecules of acetone and two of methanol. The oxygen O1 of the partial hydroxide and water species share the same space. The dimerized helicate $\{\text{I}[\text{Fe}(\text{H}_2\text{L4})_3]_2\}^{3+}$ is similar to that seen in **5** (Cl) and **7** (Br). The non-coordinated pyridine is also here interacting with OH^- or H_2O molecules to form a network of the helicate rods (see Figure 4.5). The other counterions (I_3^- and outer I^-) and solvent molecules (acetone and methanol) do not form any significant interactions with the helicate (Figure 4.20). Instead the methanol lattice molecules make hydrogen bonds with the outer I^- ions. As in the previous helicates, the Fe(II) centers exhibit the LS state at 100 K with $(\text{Fe-N})_{\text{avg}} = 1.972 \text{ \AA}$. The packing in the lattice is similar to that seen in **5**, consisting of infinite rods that are connected through $\text{O-H}\cdots\text{N}$ hydrogen bonds (Figures 4.5 and 4.6).

4.11 Magnetic Properties of

$\text{I}[\text{Fe}(\text{H}_2\text{L4})_3]_2(\text{I})_2(\text{I}_3)_{0.6}(\text{OH})_{0.4}\cdot 0.6\text{H}_2\text{O}\cdot 2\text{CH}_3\text{OH}\cdot 2\text{C}_3\text{H}_6\text{O}$ (**9**)

Magnetic susceptibility measurements of **9** were carried out on a crystalline sample in the temperature range 5-397 K, using a constant magnetic field of 0.5 T. Figure 4.19 represents the data as $\chi_M T$ vs. T plots in the heating and cooling sweeps.

The $\chi_M T$ value (*ca.* $0.30 \text{ cm}^3 \text{ mol}^{-1} \text{ K}$) below 220 K in the heating mode indicates a LS state for both Fe(II) centers with the existence of less than 5% residual HS Fe(II) centers, in agreement with the crystal structure at 100 K. The jump in the $\chi_M T$ value around 50 K mostly corresponds to the accidental presence of some oxygen during the measurements. A gradual SCO behavior was observed starting from 220 K indicated by the increase of the $\chi_M T$ value to a maximum of $3.20 \text{ cm}^3 \text{ mol}^{-1} \text{ K}$ at 397 K. This corresponds to LS \rightarrow HS SCO of *ca.* 53% of both Fe(II) centers ($\chi_M T = 6.00 \text{ cm}^3 \text{ mol}^{-1} \text{ K}$ for two Fe(II) ions, $g = 2.00$ and $S = 2$). The gradual SCO process is not complete in the temperature range available in the SQUID magnetometer up to 400 K. The temperature range and the completeness of the SCO in both compounds **8** and **9** (both with encapsulated I⁻) show similar values which indicates no important effect of the change of counterions and solvent molecules. Upon cooling, a significant change in the SCO behavior was observed, showing a more gradual transition over a range of 290 K, which again could be the result of losing solvent.

4.12 Halide-Guest Effect on the SCO

To investigate the effect of the encapsulated halide on the magnetic properties of the dimerized mononuclear helicate, $\chi_M T$ vs. T plots of compounds **5**, **7**, **8** and **9** were grouped in Figure 4.21. The dimerized helicates in these compounds are isostructural, the only significant difference being the nature of the halide- encapsulated guest inside the cavity formed by the former. The other counter ions and solvent molecules do not interact significantly with the helicates. The encapsulated halide ion in each complex forms strong hydrogen bonds with N-H group of the pyrazole rings in both mononuclear helicates. The different X \cdots H-N hydrogen bond strength in these helicates affect differently the crystal field around the iron centers and thus the SCO behavior.

As demonstrated in the $\chi_M T$ vs. T plots of Figure 4.21, the low spin state is stabilized more with stronger associated ion. The trend observed for stabilization of the LS state and therefore the increase of the SCO transition temperature was $\text{Cl}^- > \text{Br}^- > \text{I}^-$. This trend matches well the hydrogen bonding ability of the halide ions; the stronger the hydrogen bonding the more stable the LS state and higher the shift of the SCO transition temperature to higher values. The same effect of the halide guest on the SCO transition temperature was observed in the dinuclear triple-stranded helicates (compounds **1** and **2**), which was discussed in detail in chapter 3. Changing the two halide ions from

chloride to bromide in these dinuclear helicates produce a down shift in the $T_{1/2}$ of the SCO by 30 K. Here, the difference in the $T_{1/2}$ cannot be deduced since that the SCO is not complete in the temperature range available for the magnetic studies.

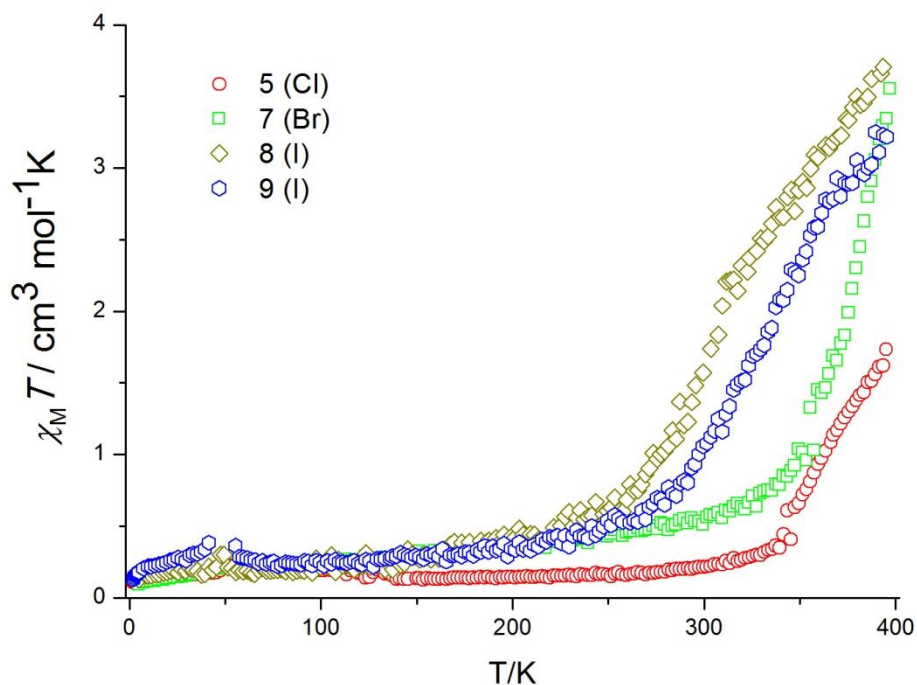


Figure 4.21: Plots of $\chi_M T$ vs. T for **5**, **7**, **8** and **9** in the heating mode showing the effect of the halide-guest on the temperature of the spin transition.

Similar effects of the halide ion on SCO were observed in other systems where the halide participates in hydrogen bonds with N-H groups of the ligand. The coordination polymers $[\text{Fe}(\text{hyetrz})_3]\text{X}_2$ (hyetrz = 4-(2'-hydroxyl-ethyl)-1,2,4-triazole) and $\text{Fe}(\text{NH}_2\text{trz})_3\text{X}_2$ (NH_2trz = 4-amino-1,2,4-triazole)³⁻⁵, the monomer $[\text{Fe}(\text{3-bpp})_2]\text{X}_2$ (3-bpp = 2,6-di{pyrazol-3-yl}pyridine) system in solution⁶ and $[\text{Fe}(\text{L})(\text{H}_2\text{bip})_2]^{2+}$ in solid state and in solution^{3,7-9} showed that the stronger the hydrogen bonding associated with the anions the more stable the LS state is. All these examples are discussed in detail in chapter 3. The reason of this behavior has not yet been fully explained.

4.13 Solution Studies of X⊂Dimerized Helicates

To investigate the behavior of X⊂dimerized Helicate in solution, ¹H NMR and ESI-MS measurements were performed in acetonitrile solutions of dissolved crystals of **5**, **7** and **8**, respectively. The helicates in these three compounds are isostructural, the only main difference being the nature of the encapsulated halide ion. Since compounds **6** and **9**

have the same cationic identity as to **5** and **8**, respectively, the former compounds were excluded from this study.

The ^1H NMR spectrum of compound **5** is shown in Figure 4.22. The resonances show paramagnetic isotropic shifts over the region 6.5 to 17 ppm. Most of the peaks also exhibit broadening, which prevents the resolution of the hyperfine coupling. In solid state, both mononuclear helicates in the dimerized structure are symmetric and they have 3-fold rotation symmetry. This yields three identical ligands in the triple stranded helicate. However, The bis-chelate ligand is coordinated to Fe(II) through one chelating site while the other site is free-of-coordination. Therefore, the C_2 symmetry of the ligand will disappear and every proton in the ligand will have a distinct environment. If the same symmetry is preserved in solution, it is expected to see 16 independent protons corresponding to the mononuclear helicate.

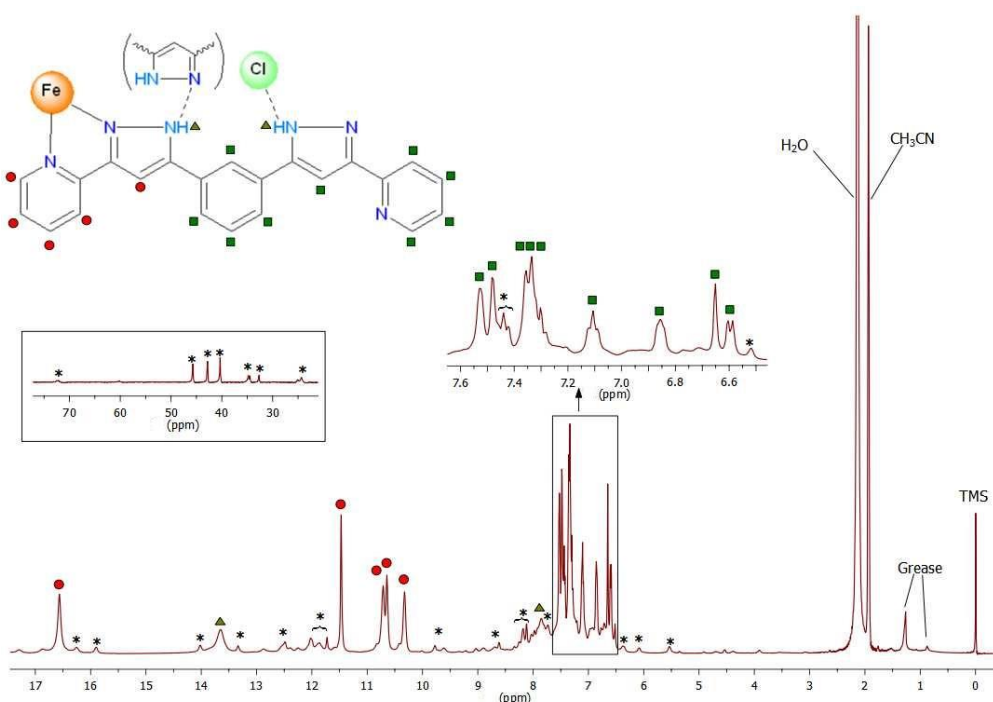


Figure 4.22: ^1H NMR of compound **5** in CD_3CN and focusing on the regions 6.5-7.5 ppm and 25-75 ppm. Tentative assignment is shown for the protons depend on the isotropic shift caused by the proximity to Fe(II) center. Peaks signed with stars correspond to minor specie or impurity (less than 9%).

Six peaks were observed in the region 10-17 ppm, five of which correspond to the aromatic protons found in the prazolyipyridine group coordinated to the Fe(II) center (red circles in Figure 4.22). The proximity to the partially HS Fe(II) induces this

isotropic shift and causes an additional broadening to these peaks. However, the isotropic shift occurs in a very narrow region in comparison to the one seen in the Cl-Fe_2 Helicate (**1**) [isotropic shift in the region -10 to 62 ppm]. This indicates a mostly LS state of the Fe(II) center in **5**, which agrees with the magnetic studies in the solid state ($\chi_M T = 0.23 \text{ cm}^3 \text{ mol}^{-1} \text{ K}$ at room temperature).

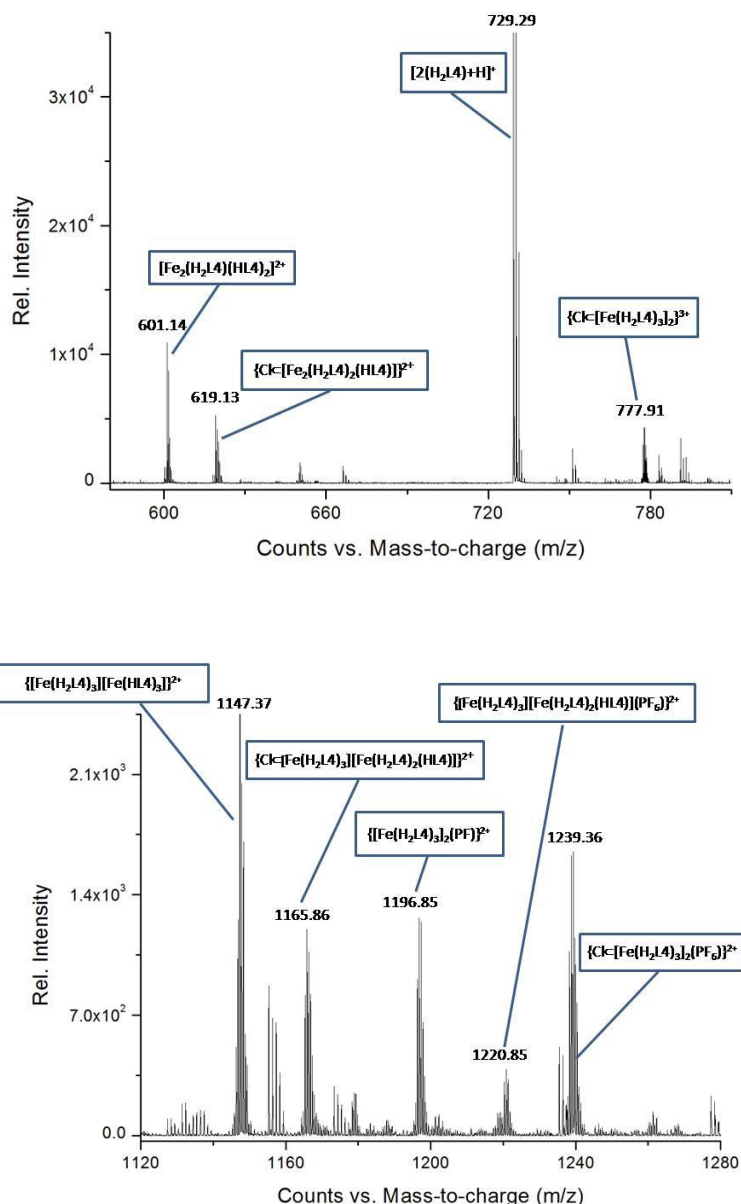


Figure 4.23: Focusing on two regions of the mass spectrum of **5** in CH_3CN . Peaks corresponding to the dinuclear helicate and the dimerized mononuclear helicate are assigned (see text for details).

The peak at 13.65 ppm mostly corresponds to one of the NH groups since it exhibit higher broadening as a result of the hydrogen bonding. The line width of this peak is more than two times larger than the one in the peak at 16.70 ppm. The second NH proton locates at 7.85 ppm, assigned because this peak has the same line width as the first NH peak at 13.65 ppm. This large difference in the isotropic shift between both NH groups is expected because of the different environment around them. First, one of these NH groups is closer to the partially HS Fe(II) center which will cause larger paramagnetic shift to this NH group. Second, the nature of the hydrogen bonding is different in both NH groups; one of them exhibits hydrogen bonding with the Cl⁻ ion while the other group is interacting with the nitrogen atom of the pyrazole ring from the neighboring ligand (see Figure 4.22).

The peaks of the nine remaining protons of the H₂L4 ligand are concentrated in the region of 6.5-7.6 ppm (green squares in Figure 4.22). These protons are far enough from the Fe(II) center to be affected and thus do not exhibit any significant paramagnetic isotropic shift. In conclusion, the expected sixteen protons for the mononuclear helicate were identified, which indicates the existence of this assembly in solution as seen in the solid state.

As discussed in chapter 3, the ¹H NMR and the mass spectrum of dissolved crystals of **1** in acetonitrile indicates the existence of an equilibrium of two metal assemblies in solution where the minor one is attributed to the dimerized mononuclear triple stranded helicate (the one isolated in solid state as compound **5**). Therefore, it is expected that dissolving crystals of **5** in acetonitrile will show also both assemblies. Indeed, mass spectrum of dissolved crystals of **5** in acetonitrile indicates both assemblies (see below). In the ¹H NMR of **5**, low intensity peaks were observed in the region 25-75 ppm (see the inset in Figure 4.22), which mostly correspond to the helical assembly since they exhibit similar paramagnetic isotropic shifts as in the Cl⁻Fe₂ Helicate (**1**). However, the high number of such minor peaks indicates more than one assembly in solution which could correspond to the empty binuclear helicate and the empty dimerized helicate in addition to the Cl⁻encapsulated one.

Parts of the mass spectrum of dissolved crystals of **5** in acetonitrile are shown in Figure 4.23. Three peaks indicate the presence of the Cl⁻encapsulated dimerized helicate at m/z = 777.19, 1165.86 and 1239.36, which correspond to {Cl⁻[Fe(H₂L4)₃]₂}³⁺,

$\{\text{Cl}[\text{Fe}(\text{H}_2\text{L4})_3][\text{Fe}(\text{H}_2\text{L4})_2(\text{HL4})]\}^{2+}$ and $\{\text{Cl}[\text{Fe}(\text{H}_2\text{L4})]_2(\text{PF}_6)\}^{2+}$, respectively. The isotopic distributions of these are consistent with the theoretical (see for example Figure 4.24).

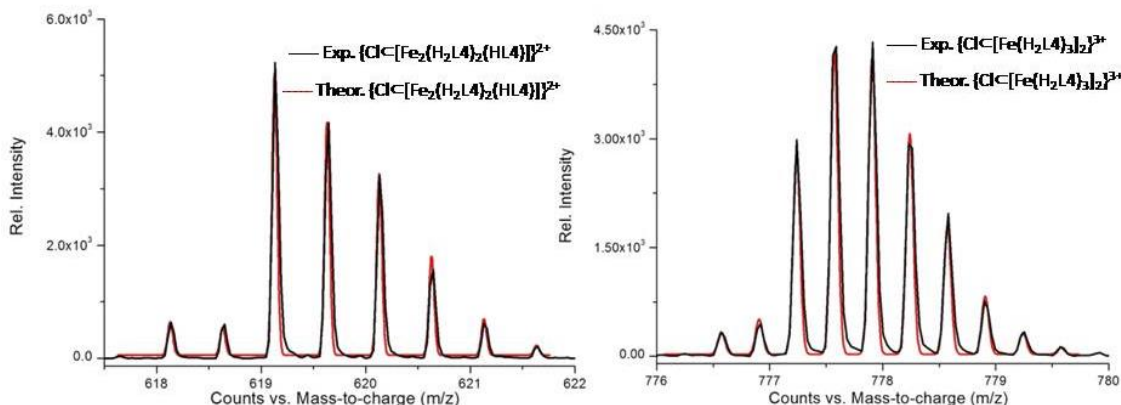


Figure 4.24: The match of theoretical and experimental isotopic distribution of the dinuclear helicate $\{\text{Cl}[\text{Fe}_2(\text{H}_2\text{L4})_2(\text{HL4})]\}^{2+}$ (left) and the dimerized mononuclear helicate $\{\text{Cl}[\text{Fe}(\text{H}_2\text{L4})_3]_2\}^{3+}$ (right) found in **5**.

Moreover, a peak corresponding to the free-of-halide dimerized helicate, namely $\{[\text{Fe}(\text{H}_2\text{L4})_3][\text{Fe}(\text{HL4})_3]\}^{2+}$ was also detected and confirmed by exact mass ($m/z = 1147.37$). In this assembly, three N-H units have been deprotonated and one iron center has been oxidized to Fe(III) during the ionization process. The peaks at $m/z = 1196.85$ and 1220.85 correspond to $\{[\text{Fe}(\text{H}_2\text{L4})_3]_2(\text{PF}_6)\}^{2+}$ and $\{[\text{Fe}(\text{H}_2\text{L4})_3][\text{Fe}(\text{H}_2\text{L4})_2(\text{HL4})](\text{PF}_6)\}^{2+}$ and indicate also the empty dimerized helical structure.

The mass spectrum of **5** indicates another metal assembly which corresponds to the dinuclear helicate (compound **1**). A peak corresponding to the Cl^- encapsulated dinuclear helicate $\{\text{Cl}[\text{Fe}_2(\text{H}_2\text{L4})_2(\text{HL4})]\}^{2+}$ at $m/z = 619.13$ was detected where one N-H unit has been deprotonated. The isotopic distribution of this peak is consistent with the theoretical one, as shown in Figure 4.24. A peak corresponding to the empty dinuclear helicate $[\text{Fe}_2(\text{H}_2\text{L4})(\text{HL4})_2]^{2+}$ was also detected and confirmed by exact mass ($m/z = 601.14$). This indicates that both assemblies are in equilibrium in solution when crystals of **5** are dissolved in acetonitrile with and without the encapsulated halide which agrees with the ^1H NMR results.

^1H NMR spectrum of dissolved crystals of compound **7** in CH_3CN is shown in Figure 4.25. The resonances exhibit paramagnetic isotropic shifts over the region 6-17 ppm

which indicates partial HS state Fe(II) centers. However, these shifts are much lower in comparison to these seen in the Br \subset Fe₂ Helicate (**2**) [isotropic shifts in the region -10 to 75 ppm], which indicates that most of the Fe(II) centers in **7** are in the LS state. This agrees with the bulk magnetic studies in the solid state at room temperature, with $\chi_M T = 0.51 \text{ cm}^3 \text{ mol}^{-1} \text{ K}$. The sixteen peaks corresponding to the H₂L4 ligand in the dimerized helicate were identified. Six peaks were observed in the region 10-17 ppm, five of which correspond to the aromatic protons of the pyrazolylpyridine group coordinated to the Fe(II) center (red circles in Figure 4.25). The broad peak at 16.01 ppm corresponds to one of the N-H groups since it exhibits high broadening (the line width for this peak is two times more than the one at 16.79 ppm). This peak shows a down-field shift by 2.36 ppm in comparison to the one seen in the **5** which indicates higher fraction of HS centers in the Br-encapsulated helicate, in agreement with solid state magnetic studies.

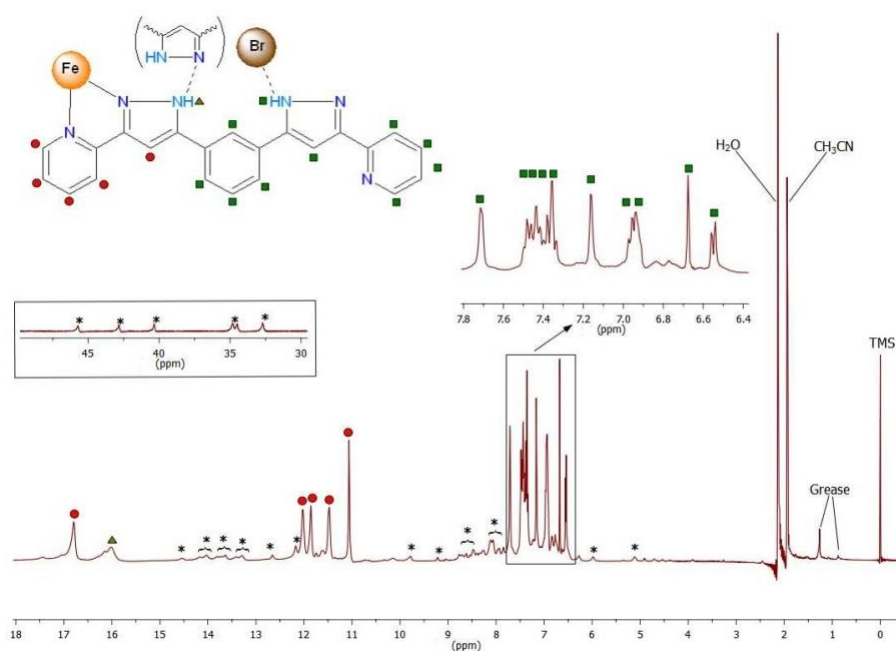


Figure 4.25: ¹H NMR of compound **7** in CD₃CN and focusing on the regions 6.4-7.8 ppm and 32-47 ppm. Tentative assignment is shown for the protons depend on the isotropic shift caused by the proximity to Fe(II) center. Peaks signed with stars correspond to minor specie or impurity (less than 9%).

The peaks corresponding to the ten remaining protons in H₂L4 are sufficiently distant from the Fe(II) center to be affected by it and thus do not exhibit any significant paramagnetic isotropic shift. These peaks are concentrated in the region of 6.5-7.8 ppm (green squares in Figure 4.25) and correspond to nine C-H aromatic protons in addition

to one N-H proton. In compound **5**, the second N-H proton was observed at 7.85 ppm while now in **7** it could not be identified as a single peak. Mostly, it is located now under the multiple broad peaks in the region 7.30-7.52 ppm.

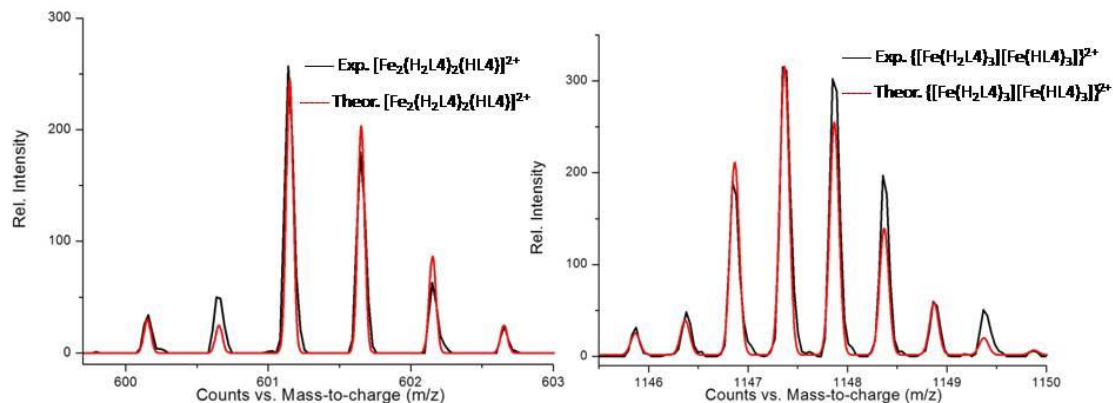


Figure 4.26: The match of theoretical and experimental isotopic distribution of the dinuclear helicate $[\text{Fe}_2(\text{H}_2\text{L4})_2(\text{HL4})]^{2+}$ (left) and the dimerized mononuclear helicate $\{[\text{Fe}(\text{H}_2\text{L4})_3][\text{Fe}(\text{HL4})_3]\}^{2+}$ (right) found in **7**. No peaks correspond to the Br-encapsulated dimerized helicate or the binuclear helicate were observed in the mass spectrum of **7**.

Minor peaks were also observed in the region 3-50 ppm, which correspond to other assemblies or impurities amounting to less than 15% of total integration. These peaks correspond to more than one assembly as indicated by the high number them with different intensities. Similarly to what seen is in **5**, one of these assemblies is the dinuclear triple stranded helicate BrCFe_2 Helicate (**2**). This agrees with the ^1H NMR spectrum of **2** in acetonitrile, which shows the two metal assemblies (**7** and **2**) and is supported by the mass spectrum of **7**, which indicates both assemblies in solution.

The mass spectrum of **7** in acetonitrile shows prominent peaks corresponding to the free ligand. However, two weak peaks were observed at $m/z = 601.14$ and 1147.37 that correspond to two distinct assemblies: empty dinuclear helicate $[\text{Fe}_2(\text{H}_2\text{L4})(\text{HL4})_2]^{2+}$ and free-of-anion dimerized helicate $\{[\text{Fe}(\text{H}_2\text{L4})_3][\text{Fe}(\text{HL4})_3]\}^{2+}$ (Figure 4.26). In agreement with the ^1H NMR results, this indicates the equilibrium between both assemblies in solution, both, full and empty of the halide. The absence of any peak corresponding to the Br-encapsulated assembly could be due to the fragility of this assembly under the conditions of ESI-MS ionization or it finds difficulty to fly under the experimental set up as seen with the ESI-MS of **2**.

The ^1H NMR for **8** in acetonitrile indicates the presence of two assemblies with equal ratio where in both of them the ligand is coordinated with one side to the metal (Figure 4.27). One of these assemblies (green squares) exhibits higher isotropic shift than the other (gray triangles) which indicate difference paramagnetic properties of Fe(II) in the two assemblies. Interestingly, no evidence of dinuclear triple-stranded helicate was observed in contrast to the Cl^- and Br^- analogous. This is clearly the result of the inability of such helicate to encapsulate I^- (Chapter 3). The two assemblies here could be the dimer helicates with and without encapsulated I^- , which affect importantly the environment around the Fe(II) and therefore change the spin state behavior of the latter. However, the mass spectra do not show any peaks correspond to metal assembly, which could be, plausibly to the difficulty to fly for these assemblies under the experimental set up.

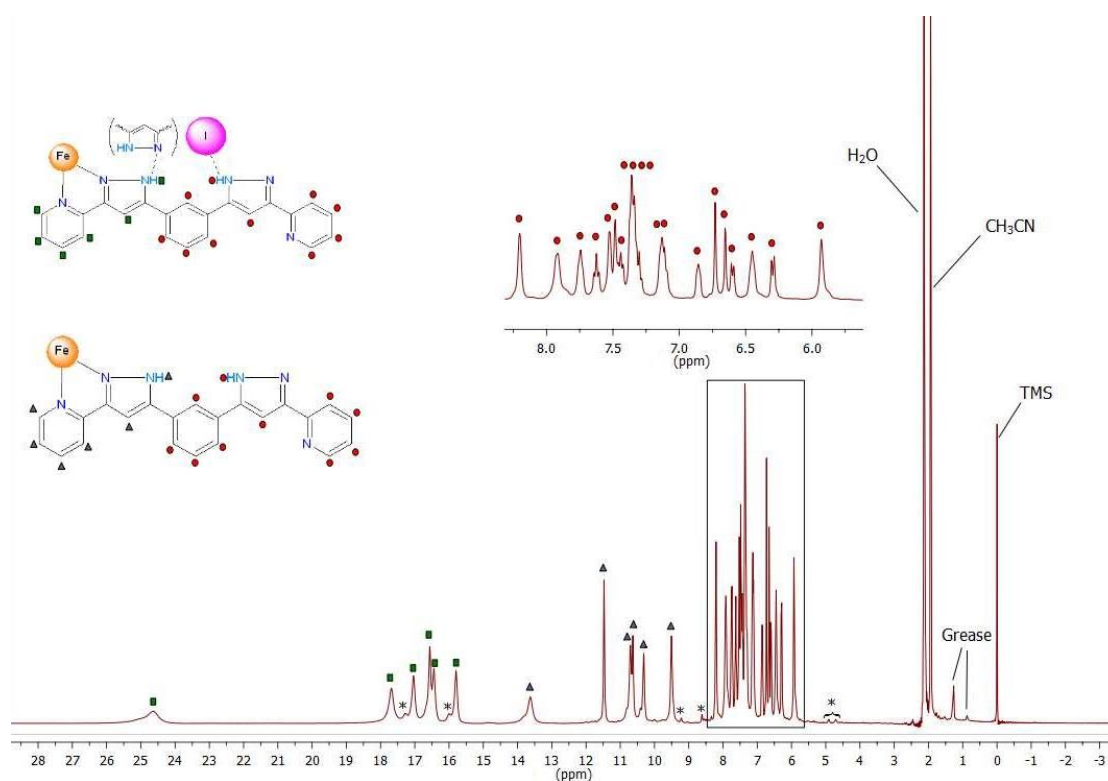


Figure 4.27: ^1H NMR of compound **8** in CD_3CN and focusing on the region 5.5–8.5 ppm.

Tentative assignment is shown for the protons depend on the isotropic shift caused by the proximity to Fe(II) center for two expected assemblies. Peaks signed with stars correspond to minor specie or impurity (less than 1%).

4.14 Conclusions

The ligand H₂L4 was successfully used to prepare dimerized mononuclear helicates $\{X\text{C}[\text{Fe}(\text{H}_2\text{L4})_3]_2\}^{3+}$ which have the ability to encapsulate halide ions in a central cavity. The assemblies are stabilized by numerous supramolecular interactions: strong hydrogen bonds with the encapsulated halides and strong hydrogen bonds (N-H...N) and π - π interactions between the intertwined ligands. These helicates exhibit gradual and incomplete (up to 400 K) SCO which start above 250 K. The nature of the halide affects the SCO in these helicates where the stabilization of the LS state follow this trend $\text{Cl}^- > \text{Br}^- > \text{I}^-$. These helicates are stable in solution as shown by ¹H NMR and ESI-MS studies. However, an equilibrium in solution is evident between these assemblies and the dinuclear triple stranded helicates $\{X\text{C}[\text{Fe}_2(\text{H}_2\text{L4})_3]\}^{3+}$ where both species are present in solution to different extents in addition to the ones with free of encapsulated halide. Using the same ligand and the same iron and halide source (FeX₂), different host-guest supramolecular chemistry can be favored in solid state by slight change in the synthesis conditions.

4.15 Experimental

ClC[Fe(H₂L4)₃]₂(OH)(PF₆)₂·H₂O (5). A suspension of H₂L4 (25 mg, 0.069 mmol) in methanol (7 mL) was added dropwise to a methanolic solution (3 mL) of FeCl₂·4H₂O (9.1 mg, 0.046 mmol). A red solution formed which was stirred for 45 minutes and then filtered off. The resulted solution was layered with aqueous solution (10 ml) of NH₄PF₆ (7.5 mg, 0.046 mmol) which yielded red crystals after a few days. The yield was 3.6 mg (12.1 %). *Anal. Calc.* (Found) for **5** (+H₂O, +5CH₃OH): C, 57.82 (58.23); H, 4.32 (3.91); N, 17.72 (17.32). ESI-MS: *m/z* 777.19 [Fe(H₂L4)₃Fe(H₂L4)₃Cl]³⁺, *m/z* = 1147.37 [Fe(H₂L4)₃Fe(HL4)₃]²⁺, *m/z* 1165.86 [Fe(H₂L4)₃Fe(H₂L4)₂(HL4)Cl]²⁺, *m/z* 1196.8 [Fe(H₂L4)₃Fe(H₂L4)₃PF₆]²⁺, *m/z* 1220.8 [Fe(H₂L4)₃Fe(H₂L4)₂(HL4)PF₆]²⁺, *m/z* 1239.36 [Fe(H₂L4)₃Fe(H₂L4)₃CIPF₆]²⁺.

ClC[Fe(H₂L4)₃]₂(FeCl₄)₃·2C₃H₆O·4C₇H₈ (6). A suspension of H₂L4 (25 mg, 0.069 mmol) in acetone (10 mL) was added dropwise to a solution (5 mL) of FeCl₂·4H₂O (13.6 mg, 0.069 mmol) in acetone. A red solution formed which was stirred for 1 hour and then filtered off. The resulted solution was layered with toluene which yielded red

crystals after a few days. The yield was 1.6 mg (3.4 %). *Anal. Calc.* (Found) for **6** ($-3\text{C}_7\text{H}_8 + 3\text{H}_2\text{O}$): C, 54.61 (54.40); H, 3.86 (3.59); N, 15.81 (15.62).

$\text{Br} \cdot [\text{Fe}(\text{H}_2\text{L4})_3]_2(\text{OH})(\text{PF}_6)_2 \cdot \text{H}_2\text{O}$ (7). A suspension of $\text{H}_2\text{L4}$ (25 mg, 0.069 mmol) in methanol (7 mL) was added dropwise to a methanolic solution (3 mL) of FeBr_2 (13.5 mg, 0.046 mmol). A red solution formed which was stirred for 45 minutes and then filtered off. The resulted solution was layered with aqueous solution (10 ml) of NH_4PF_6 (7.5 mg, 0.046 mmol) which yielded red crystals after a few days. The yield was 3.9 mg (12.5 %). *Anal. Calc.* (Found) for **7** ($+7\text{H}_2\text{O}$): C, 55.69(55.27); H, 4.07 (3.65); N, 17.71 (17.35). ESI-MS: m/z 1147.37 $[\text{Fe}(\text{H}_2\text{L4})_3\text{Fe}(\text{HL4})_3]^{2+}$.

$\text{I} \cdot [\text{Fe}(\text{H}_2\text{L4})_3]_2(\text{PF}_6)_{2.23}(\text{I})_{0.21}(\text{I}_3)_{0.56} \cdot 2\text{CH}_3\text{OH}$ (8). A suspension of $\text{H}_2\text{L4}$ (25 mg, 0.069 mmol) in methanol (20 mL) was added dropwise to a methanolic solution (5 mL) of FeI_2 (14.3 mg, 0.046 mmol). A red solution formed which was stirred for 45 minutes and then filtered off. The resulted solution was treated with a methanolic solution (5 ml) of NH_4PF_6 (7.5 mg, 0.046 mmol). The solution was left for slow evaporation at ambient temperature which yielded red crystals after a few days. The yield was 2.5 mg (7.1%). *Anal. Calc.* (Found) for **8** ($+2\text{H}_2\text{O}$): C, 52.11(51.82); H, 3.52 (3.34); N, 16.33 (16.43).

$\text{I} \cdot [\text{Fe}(\text{H}_2\text{L4})_3]_2(\text{I}_2)(\text{I}_3)_{0.6}(\text{OH})_{0.4} \cdot 0.6\text{H}_2\text{O} \cdot 2\text{CH}_3\text{OH} \cdot 2\text{C}_3\text{H}_6\text{O}$ (9). A suspension of $\text{H}_2\text{L4}$ (25 mg, 0.069 mmol) in methanol (10 mL) was added dropwise to a methanolic solution (5 mL) of $\text{Fe}(\text{CF}_3\text{SO}_3)_2 \cdot 6\text{H}_2\text{O}$ (10.4 mg, 0.023 mmol). A red solution formed which was stirred for 30 minutes and then filtered off. The resulted solution was treated with methanolic solution (5ml) of 5-fold excess of NBu_4I which yielded a heavy precipitate. The solid was collected and then dissolved in hot nitromethane. The red solution was vapor diffused with ethylacetate which yielded red crystals after few days. The yield was 1.5 mg (4.2 %). *Anal. Calc.* (Found) for **9** ($-2\text{CH}_3\text{OH}$): C, 54.50 (54.62); H, 3.63 (3.51); N, 16.58 (16.97).

4.16 References

- 1 T. Shiga, E. Oshiro, N. Nakayama, K. Mitsumoto, G. N. Newton, H. Nishikawa and H. Oshio, *Eur. J. Inorg. Chem.*, 2013, 781–787.
- 2 J. Rebek, *Acc. Chem. Res.*, 2009, **42**, 1660–8.
- 3 M. A. Halcrow, *Chem. Soc. Rev.*, 2011, **40**, 4119–4142.
- 4 Y. Garcia, P. J. van Koningsbruggen, René Lapouyade, L. Rabardel, O. Kahn, M. Wieczorek, R. Bronisz, Z. Ciunik and M. F. Rudolf, *Mol. Inorg. Chem.*, 1998, **1**, 523–532.
- 5 L. A. Sheludiyakova and S. V Larionov, *Russ. J. Coord. Chem.*, 2003, **29**, 22–27.
- 6 S. A. Barrett and M. A. Halcrow, *RSC Adv.*, 2014, **4**, 11240.
- 7 Z. Ni and M. P. Shores, *J. Am. Chem. Soc.*, 2009, **131**, 32–33.
- 8 Z. Ni and M. P. Shores, *Inorg. Chem.*, 2010, **49**, 10727–35.
- 9 Z. Ni, A. M. McDaniel and M. P. Shores, *Chem. Sci.*, 2010, **1**, 615.

